Experiments in Fluids (2022) 63:173
https://doi.org/10.1007/s00348-022-03518-2

RESEARCH ARTICLE

Measurement of instantaneous fully 3D scalar dissipation rate in a turbulent swirling flow

Irfan A. Mulla[1] · **Yannis Hardalupas**[2]

Received: 17 July 2021 / Revised: 16 September 2022 / Accepted: 26 September 2022 / Published online: 3 November 2022

Abstract
This paper describes the measurement methodology for quantifying the instantaneous full 3D scalar dissipation rate (SDR or χ) in order to characterize the rate of mixing. Measurements are performed in a near field of a jet-in-swirling-coflow configuration. All three components of χ are measured using a dual-plane acetone planar laser-induced fluorescence technique. To minimize noise, a Wiener filtering approach is used. The out-of-plane SDR component (χ_3) is validated by assuming isotropy between axial and azimuthal components of SDR. An optimum laser-sheet separation distance (Δs) is identified by comparing the SDR components on the basis of instantaneous, mean, and probability density function data. The in-plane resolution needs to match the Batchelor scale (λ_B) for the central difference scheme-based SDR deduction. However, the out-of-plane resolution, Δs, requirement is different owing to the use of two-point difference based SDR and systematic biases. The optimum Δs is found to be $2.5\lambda_B$. Finally, measurement guidelines are provided to assess the accuracy of 3D SDR measurements.

1 Introduction

Low emission non-premixed or partially premixed combustion requires air–fuel mixing to occur at a certain rate and proportion. Air–fuel mixing in gas turbine combustors and industrial burners is frequently achieved through turbulent swirling flows. Such flows, besides mixing, also facilitate flame stabilization owing to a swirl-induced recirculation zone near the burner exit. The key combustion characteristics, such as flame stabilization and pollutant formation, are influenced by the rate of air–fuel mixing. Thus, an understanding of the turbulent mixing process is of practical significance.

The degree of air–fuel mixing can be characterized by a conserved scalar, such as the concentration of passive species or mixture fraction. The rate at which scalar fluctuations dissipate can be estimated using the scalar dissipation rate (SDR) term, which is expressed as $\chi \equiv 2D\nabla\zeta.\nabla\zeta$, where D is the molecular diffusivity and ζ is a conserved scalar. χ^{-1} can be interpreted as a diffusion time scale (or χ as a rate of molecular mixing), imposed by a given mixing field (Peters 1983). Consequently, χ is of significance in modelling non-premixed or partially premixed turbulent combustion, especially for ignition and flame extinction, as used in flamelet models (Peters 1998). χ values can be obtained from the scalar field which could be deduced from computations or measurements. SDR has been evaluated using data from direct numerical simulation (DNS) in turbulent round non-reacting jets (Vlad 2021) and planar jet flames (Hawkes et al. 2009; Chakraborty et al. 2013). Numerical computations of practical turbulent flames at high Reynolds number (Re) are generally not feasible due to the need to resolve the finer length scales. Conversely, experimental measurements appear promising due to the following reasons. Firstly, there are no direct consequences of not resolving the finest scales on flow characterization over a chosen range of scales (Dimotakis 2005). Secondly, the finest scales can be resolved with current advances in optical techniques. Additionally, non-homogeneous and spatially developing turbulent flows (which cannot be readily simulated/modeled) can be investigated through measurements. Nonetheless, DNS or theoretical analysis can provide useful relationships or insights to facilitate experimental deduction of the full three-component SDR, as discussed subsequently.

✉ Irfan A. Mulla
irfanmulla@iisc.ac.in

[1] Department of Aerospace Engineering, Indian Institute of Science, Bangalore 560012, India

[2] Department of Mechanical Engineering, Imperial College London, London SW7 2AZ, UK

The scalar dissipation rate in turbulent gas-phase non-reacting flows has been measured by several research groups to quantify the rate of mixing. To estimate χ, conserved scalar (ζ) could be based either on temperature or concentration. Typically, the mole fraction is used as a conserved scalar in non-reacting flows, whereas the mixture fraction is used in reacting flows to deduce χ. Note that to evaluate the $\nabla\zeta$ term (for χ estimation), the scalar gradients in all three directions are needed. Most of the past measurements were limited to either one or two dimensions, which consequently restricted χ evaluation to one or two components (χ_{2C}). The reported flow configurations included round jets (Mi et al. 1995; Tsurikov and Clemens 2002), planar jets (Su and Clemens 1999; Kothnur and Clemens 2005), starting jets (Soulopoulos et al. 2015), axisymmetric plumes (Markides and Mastorakos 2006), turbulent wake (Chen et al. 2020), and turbulent swirling flows (Stetsyuk et al. 2016; Feikema et al. 1996). Feikema et al. (1996) reported SDR measurements in three flow configurations, namely round turbulent jet, jet with coflowing non-swirling air, and jet with coflowing swirling air. 2D measurements were made from which the full SDR was obtained by assuming isotropy between radial and azimuthal components of SDR. Mean SDR for the jet in a swirling coflow measured nearly twice as of a simple jet flow case. The authors concluded that the higher mean SDR values in the swirling flow were due to an increase in the number of SDR layers in space and not due to higher values of SDR within a given SDR layer. The presence of a swirl enhances the rate of mixing through an increase in the number of mixture fraction gradient surfaces through azimuthal distortion. An instantaneous peak SDR across three flow conditions was reported to be of a similar magnitude.

SDR in reacting gas-phase flows has been measured by a few research groups. Such evaluation is extremely difficult as it requires multi-scalar measurements (Karpetis and Barlow 2002; Fuest et al. 2018). Thus, an indirect estimate of χ based on certain marker species was proposed (Bijjula and Kyritsis 2005). In a turbulent flame, imaging of χ was achieved (Sutton and Driscoll 2013) through NO molecule which was shown to be passive in CO flames. In a turbulent hydrocarbon flame, imaging of Krypton gas concentration has been demonstrated to provide the quantitative mixture fraction (Hsu et al. 2011) and scalar dissipation rate (Park et al. 2019). Mixing in liquid-phase turbulent flows has also been investigated (Dahm et al. 1991; Buch and Dahm 1996) through χ evaluation.

Although several measurements of SDR have been reported in the past, data is generally prone to uncertainties. There are two main sources of error, namely finite resolution and noise, that together determine the accuracy of measured SDR. The influence of these factors on SDR has been studied in great depth. The resolution requirement is compared with the smallest scale. The smallest characteristic scale for scalar mixing is considered to be the Bachelor scale (λ_B). Thus, it is necessary to compare λ_B with the measurement resolution. For measurements, wire-based probes or laser-based techniques are used. In wire-based scalar (temperature) measurements, generally, the wire diameter is small, but the length could exceed λ_B. The impact of wire length has been investigated using a modeled dissipation spectrum (Wyngaard 1971). This analysis indicated that to measure SDR within 10% accuracy, the wire length should be less than $2\lambda_B$. To account for a finite wire length, a correction approach was proposed by considering isotropy and a modeled spectrum. A single wire cannot directly provide spatial gradients for which two parallel wires have been used. In the case of two-wire measurements, the influence of wire spacing on SDR has been assessed by Antonia and Mi (1993a) using a measured 1D spectrum and isotropy assumption. To measure SDR within 10% of its true value, a resolution requirement of $2\lambda_B$ was noted, similar to Wyngaard (1971). Apart from wire-based measurements, the impact of resolution on SDR in laser-based measurements has also been investigated. For planar measurements, the influence of in-plane and out-of-plane resolutions was studied by Kaiser and Frank (2011). The in-plane resolution is generally determined by imaging optics and camera pixel spacing, whereas the out-of-plane resolution is governed by the laser-sheet thickness. SDR was shown to be much more sensitive to the in-plane resolution degradation than the out-of-plane resolution degradation. Consequently, the resolution requirements in the direction of the gradient (in-plane) and in the orthogonal direction (out-of-plane) are different. A model was developed to provide a relationship between in-plane and out-of-plane resolution requirements for equal SDR sensitivity to both resolution parameters (Kaiser and Frank 2011).

Inadequate resolution tends to underestimate SDR, whereas excessive noise overestimates SDR relative to its true value. Therefore, both the effects were studied together by Wang et al. (2007b) through a system model. The model also considered data filtering and numerical stencil that is used to obtain the scalar gradient. In the presence of noise, enhanced resolution generates a large positive bias in the measured SDR. The identical observations have been reported in wire-based measurements, where wire spacing less than $2\lambda_B$ was found to increase noise contribution significantly (Antonia and Mi 1993b). In another study by Danaila et al. (2000), the optimum wire separation was determined to be $3\lambda_B$. Such estimates are not necessarily universal since measurements can have different noise/bias characteristics. For a noise-free case, the resolution requirement of $\pi\lambda_B$ was suggested (Wang et al. 2007).

For laser-based measurements, the resolution requirement could be satisfied for moderate Reynolds number flows; however, measurement noise cannot be avoided. The main contribution comes from the photon shot noise. To evaluate the scalar gradient, generally, noise needs to be filtered out.

Different approaches have been used to reduce noise from an imaged scalar field. An interlacing approach has been reported by Kaiser and Frank (2007) to reduce noise in mean SDR. In this technique, power spectral densities (PSDs) for even and odd rows of a given image are evaluated. Since the noise is uncorrelated between adjacent rows, the noise in the mean spectrum cancels when both (odd/even rows) PSDs are considered. This approach is useful for obtaining the mean SDR from PSD. Note, such noise reduction is feasible only when the scalar field is spatially over-resolved (Kaiser and Frank 2007). For instantaneous SDR deduction from single-shot data, image smoothing is needed. The reported smoothing methods include median, adaptive Wiener, and wavelet filtering (Markides and Mastorakos 2006), and Gaussian kernel smoothing (Kaiser and Frank 2007, 2011). Krawczynski et al. (2006) compared different filtering approaches, namely Gaussian, adaptive Wiener, and frequency filters. In frequency filtering (Miller and Dimotakis 1991, 1996), beyond a certain cut-off frequency, a noise-contaminated part of the spectrum is replaced by a modeled spectrum. The composite (measured and modeled) spectrum is utilized to design an optimal filter which in turn is used to remove the noise from instantaneous images. Based on the decay of the dissipation spectrum, it was found that the frequency filtering was superior to other filtering approaches. An identical frequency filtering approach has been implemented by Soulopoulos et al. (2014) where the designed filter was referred to as an optimal Wiener filter, following Miller and Dimotakis (1991). The present work utilizes a similar technique to design a Wiener filter.

To measure scalars, a non-intrusive in-situ approach is preferred. The laser-based techniques include Raman scattering for multi-species measurements, Rayleigh scattering either for a species or temperature measurement, and laser-induced fluorescence (LIF) for species concentration. Early measurements were one-dimensional. Eventually, with the advances in lasers and cameras, two-dimensional (i.e., planar) Rayleigh and LIF techniques became established. In the planar LIF (PLIF) technique, a tracer can be seeded in one of the streams to mark the conserved scalar, ζ. From a PLIF image, gradients only in two in-plane directions are accessible, which consequently limits χ evaluation to two components (χ_{2C}). Note that even the evaluation of χ_{2C} is a challenging task due to measurement noise and limited spatial resolution, as discussed above. Consequently, the accuracy assessment of χ is a very difficult task. These difficulties are well recognized in the turbulent non-reacting (Ghandhi 2006) and reacting (Fuest et al. 2018) flow communities. Despite these challenges, a few researchers measured all three components of χ, for instance, in non-reacting gas-phase planar jets (Su and Clemens 1999), liquid-phase flows (Dahm et al. 1991), and in reacting flows (Karpetis and Barlow 2005). The out-of-plane gradient was obtained through multi-planar imaging of ζ. However, as discussed by Bilger (2004), such measurements can contain appreciable uncertainty.

Since the full 3D SDR measurements are susceptible to errors, previous studies have estimated the full SDR (χ) from 1D or 2D measurements. If local isotropy is assumed, then the mean full SDR can be deduced simply as, $\langle\chi\rangle = 3\langle\chi_{1C}\rangle$, where χ_{1C} is a single component SDR obtained from 1D measurements. However, with this approach, the resulting PDF of χ deviated from the well-established log-normal profile (Dahm and Buch 1989). Therefore, Dahm and Buch (1989) developed a relationship to reconstruct a PDF of the full SDR from 1D measurements through the assumption of the isotropic scalar field. The distribution of the full SDR was found to be log-normal. This analysis was extended further by Hawkes et al. (2009) by replacing the isotropic assumption with an assumed distribution of the scalar gradient vector orientation. Through the developed analysis, the mean and variance of full SDR were related to its lower-order (1D or 2D) projections by assuming the log-normal distribution of χ. This analysis was validated against DNS data of turbulent planar jet flames. Based on this agreement, the developed relationships were used to reconstruct PDF of χ from the measured 1D and 2D scalar data for a planar jet flame. The shapes of reconstructed PDFs were close to the log-normal profile, similar to the DNS data. A similar analysis was performed by Chakraborty et al. (2013) where a relationship for the full SDR was presented from 2D SDR, as $\langle\chi\rangle = 3/2 \times \langle\chi_{2C}\rangle$. The authors assumed the isotropic distribution of the PDF of scalar gradient orientation angle. The developed expressions were verified against the DNS data of a planar turbulent flame. In an anisotropic field, instead of assuming a particular distribution of scalar gradient orientation, the measurement can be performed through multi-planar imaging. In turbulent non-premixed flames (Karpetis and Barlow 2005; Cutcher et al. 2018), the radial component of SDR and measured local flame-normal vector were used to obtain the full SDR.

In turbulent swirling flows of practical relevance, so far, only the χ_{2C} measurements have been reported (Feikema et al. 1996; Stetsyuk et al. 2016). These flows are highly three-dimensional, and thus a direct three-component (3C) measurement of χ is desired. The present work reports planar 3C scalar dissipation rate measurements in a turbulent swirling flow for the first time. The measurements are performed in the developing near-field region of the flow. The near-field properties are important since they govern the stabilization (and local extinction) of the flame. Such near-field measurements of χ are difficult since the dissipation length scales are the smallest, which consequently necessities a high spatial resolution. The dual-plane acetone-PLIF technique is used to image the ζ field in three dimensions, from which χ is evaluated. Although

dual-plane measurements have been reported in the past (Su and Clemens 1999; Dahm et al. 1991; Karpetis and Barlow 2005), the influence of laser-sheet separation distance has not been rigorously analyzed in previous studies. As noted earlier from parallel wire measurements (Antonia and Mi 1993b; Danaila et al. 2000), a smaller separation distance ($< 3\lambda_B$) could introduce noise biases in the measured SDR. In the present work, we assess the accuracy of the out-of-plane SDR component as a function of the separation distance between measurement planes. We present the measurement technique, data reduction method, and validation approach to evaluate the full three-component χ in a turbulent swirling flow. The out-of-plane component of χ is rigorously validated through several approaches. This paper provides guidelines to measure and validate χ in high Reynolds number flows using the dual-plane imaging technique.

2 Methodology

2.1 Flow facility

A turbulent non-reacting swirling flow was generated using an existing swirl burner. The details of this facility are available in the following Refs. (Stetsyuk et al. 2016; Stetsyuk 2014). The setup consisted of a central jet (intended for fuel) which is surrounded by a swirling air coflow, as illustrated in Fig. 1. The central tube has an internal diameter, d of 15 mm and a wall thickness of 1.5 mm. The outer tube has an internal diameter, Da of 50.8 mm. The central tube terminates 8 mm upstream of the outer tube. The coordinates are defined at the exit plane of the central tube, along the axis, as illustrated in Fig. 1. The swirl was generated within the annular coflow. To control the swirl intensity, air coflow was divided into two parts, namely tangential and axial. The axial-air stream does not contain any swirl generator, while the tangential-air stream passes through a swirler containing six tangential slots. Further details of the burner geometry can be found in Ref. (Stetsyuk 2014).

The swirling flow was established at atmospheric pressure. Instead of fuel, the air was supplied to the central jet stream at a rate of $Q_c = 40$ liters per minute (lpm). Since the air was seeded with acetone ($\approx$ 19.4%), the total flow rate was approximately 48 lpm, which translates to the area-averaged bulk velocity of 4.5 m/s. Details of acetone seeding are provided subsequently. To generate a turbulent swirling flow, air flow rates through an annular opening were set as follows: tangential air, $Q_t = 400$ lpm, and axial air, $Q_a = 390$ lpm. The flow through this facility was characterized by the swirl number and bulk Reynolds number (Re). The swirl number is defined as $S = 2G_\theta/G_z Da$, where G_θ and G_z are the axial fluxes of angular and axial momentum, respectively. To calculate momentum, the axial and tangential components of velocity are needed. A previous work (Milosavljevic 1993) measured the corresponding velocities for imposed Q_a and Q_t flow rates, based on which the swirl numbers were determined. Three swirl numbers were obtained in Refs. (Milosavljevic 1993; Stetsyuk et al. 2016) by varying the ratio of Q_t/Q_a, at a constant total ($Q_a + Q_t$) air flow rate. Based on this characterization, for the present flow conditions, the swirl number (S) is estimated to be 0.4. The overall effect of a swirl is to increase the jet spread. Depending upon the degree of swirl, flows can be classified in low ($S <\simeq 0.4$) and high ($S >\simeq 0.6$) swirl regimes (Lilley 1977). This classification is primarily based on the formation of a central toroidal recirculation zone (CTRZ) at $S \simeq 0.6$. At a low swirl number, CTRZ is not formed. In the present case, only the annular flow has been imparted with a swirling motion. The absence of swirl in the central jet and low swirl number of annular flow results mainly in an increase in the jet spread

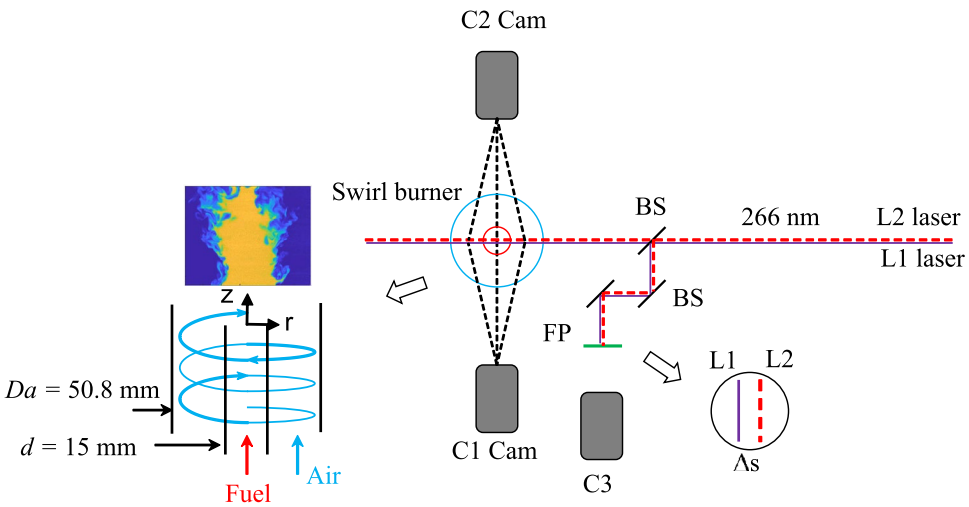

Fig. 1 Optical layout of dual-plane acetone-PLIF setup. L: laser, C: Camera, BS: beam sampler, and FP: fluorescent acrylic plate. A schematic of the swirl flow facility with a coordinate system is shown on the left. The area-averaged nominal velocity magnitude through the central jet is 4.5 m/s and through the annulus is 7.4 m/s

without the formation of CTRZ. The central jet is expected to have a negligible mean azimuthal velocity component, while the annular flow has swirl-induced azimuthal velocity. This leads to a rotational shear that enhances mixing between two streams. The difference in axial velocity components of the central jet and annular stream also assist in mixing through convective transport across the shear layer.

For the present flow, Re is estimated to be 24000, based on the bulk velocity ($V \approx 7$ m/s) obtained for a total flow rate ($Q_c + Q_a + Q_t$) and outer tube diameter (Da). For non-swirling shear flows, the local Reynolds number (Re_δ) based on the shear layer thickness and velocity difference has been used, for instance, in Slessor et al. (1998). In the present swirling flow, Re_δ could not be obtained precisely since the velocity measurements were not performed for the present test case. Nonetheless, based on past measurements (Milosavljevic 1993) on the identical burner at $z = 12$ mm, we estimate Re_δ of 3000. This value is based on the interpolated azimuthal velocity difference at a swirl number of 0.4 and the shear layer width measured from the present data (as 2–98% of peak X_f). For a given total flow rate, with varying swirl numbers, Re would remain constant, but Re_δ would vary. Thus, for turbulent mixing in the shear layer, Re_δ is more relevant than Re.

The mixing between the central jet and the swirling coflow is characterized by the mole fraction of the central jet air. This quantity is a conserved passive scalar (ζ) for non-reacting flows. To measure the mole fraction, the acetone-PLIF technique was employed. The air was seeded with acetone vapor using a bubbler. Due to the continuous evaporation of acetone, the temperature of the acetone bubbler can decrease. Therefore, the bubbler was kept in a constant temperature hot water bath at 30 °C. This arrangement ensured a steady-state acetone vapor concentration in the jet stream. No drift in the acetone-PLIF signal was noted over a test duration (800 images over 80 s), suggesting a steady-state acetone concentration. At 30 °C temperature, the saturation acetone concentration calculated using the vapor pressure is around 37.5%. The temperature of the air/acetone mixture is not necessarily 30 °C. In the present experiments, mixture temperature was not measured. Nonetheless, an acetone concentration estimate can be obtained by observing the attenuation of the PLIF signal in the acetone-seeded uniform part of the jet. Such a uniform region exists near the jet exit in both laminar and turbulent flow conditions. The considered uniform region was from $z = 11.4$ to 13.7 mm and from $r = -2$ to +2 mm. To reduce noise influence, LIF signal values were averaged vertically (over 2.4 mm height). The axially averaged radial extinction profile was fitted with the exponential function. The fitted function was used to deduce the acetone concentration. To extract the concentration value, the Beer-Lambert law was considered (e.g., Wagner et al. (2009)). The absorption cross section value of 4.36×10^{-24} m^2 (relevant to 266 nm) was used (Frackowiak et al. 2008). At a relatively low air flow rate of 5 lpm through the bubbler, the attenuation-based acetone concentration value is 37.1%, which is quite close to the vapor pressure based value. However, at a high air flow rate of 40 lpm, the attenuation-based acetone concentration value is 19.4%. Recall that no drift in the PLIF signal was noted over the test duration. This suggests that despite the use of a constant temperature hot water bath, depending upon the air flow rate, a dynamic equilibrium is reached at a certain intermediate temperature. Note, the bubbler inlet air flow rate of 40 lpm becomes 48 lpm of air/acetone mixture at the jet exit.

2.2 Dual-plane PLIF

A dual-plane acetone-PLIF system was set up to obtain all three components of the gradient of the conserved scalar (i.e., mole fraction). The dual-plane approach has been used by Yip and Long (1986) and Su and Clemens (1999) to obtain all three components of the scalar gradient. In the past (Su and Clemens 1999), the acetone-PLIF was used in combination with Rayleigh scattering to avoid the signal cross-talk between two planes. The Rayleigh scattering technique is not preferred (relative to acetone-PLIF) due to—(1) a stringent requirement of the flow to be particle/dust-free since particles can cause Mie scattering interference in the Rayleigh signal, and (2) the requirement of sufficient contrast of Rayleigh scattering cross section between the jet and surrounding fluids, which motivated the use of propane jet in Su and Clemens (1999). Our present approach utilizes air in both the central jet and annular flow, which simplifies the experiment. The acetone-PLIF approach is preferred since a high signal-to-noise ratio (SNR) can be obtained at relatively low laser pulse energy. Additionally, the broadband absorption spectrum of acetone permits the use of the readily accessible fourth harmonic (266 nm) of the Nd:YAG laser. Since the acetone-PLIF signal can be sufficiently strong, an intensified camera is not necessary. Therefore, besides the cost-benefit, by using an unintensified CCD camera, noise associated with the intensifier can be eliminated. A cross-talk of the PLIF signals between the planes can be avoided through a sub-microsecond delay between image acquisitions.

To facilitate a statistical analysis, 1600 image pairs were acquired at a 10 Hz repetition rate in two consecutive runs (of 800 images each). Figure 1 shows the schematic of the optical layout. Two Laser/Camera pairs, labeled as L1/C1 and L2/C2, constituted two independent PLIF systems. This setup provided mixing fields in two adjacent planes separated by an out-of-plane distance, Δs. Δs is defined as the peak-to-peak distance between two laser sheets. PLIF images acquired from L1/C1 and L2/C2 systems are denoted

as I1 and I2, respectively. The laser sheets were separated in time by 0.8 µs, which is small enough (compared to the flow time-scale) to facilitate quasi-simultaneous imaging. This time delay was necessary to avoid the cross-talk of PLIF signal between cameras C1 and C2, as the minimum exposure time was limited to 1 µs for the used CCD cameras.

Two datasets were obtained; one with mean $\Delta s = 304$ µm and another with mean $\Delta s = 109$ µm. Between these two campaigns, laser energy and C3 camera (used for Δs deduction) parameters were optimized. These variations are stated subsequently.

2.2.1 Laser sheets

Acetone molecules seeded in the air were excited using the fourth harmonic (266 nm) of a Nd:YAG laser. Two of the four sets of a multi-channel Nd:YAG laser (Thales) were used to obtain two laser beams. A single laser channel/unit consisted of an oscillator and an amplifier, which generated the laser beam with 1064 nm wavelength and 9 mm beam diameter. The Thales laser bench included optical elements that generate second harmonics (532 nm) from each laser channel. These 532 nm beams from each of the four channels were recombined in space using a set of mirrors. The overlapped beams were passed through a single fourth harmonic generation unit. The output of this stage contained a minor laser residual at 532 nm (despite the wavelength separation through two dichroic mirrors), which can interfere with the PLIF signal. This issue was resolved by using a Pellin-Broca prism (at the laser exit), which separated the 532 nm residual light from 266 nm. Next, the laser beams were converted to a sheet by using a spherical ($f = 1000$ mm) and a cylindrical ($f = -75$ mm) lenses. The resulting sheets were ~45 mm wide and ~0.11 to 0.14 mm thick (FWHM). A detailed characterization of the laser sheet is provided subsequently. A central portion of the sheet (25 mm wide) was used for imaging the acetone-PLIF signal. Beams from L1 and L2 lasers were aligned in the vertical plane. The horizontal (normal to the imaging plane) separation (see Δs in Fig. 1) was achieved by manipulating the beam recombination mirrors. This approach provided a robust control of Δs. The laser beam travel from the laser exit to the measurement plane was approximately 3 m. A shot-to-shot beam pointing instability exists in lasers, which could result in fluctuations of Δs. Thus, Δs was monitored on a shot-to-shot basis by a third camera (labeled as C3 in Fig. 1). A fraction of the light-sheet was sampled using a set of beam samplers (BSF-10UV, Thorlabs). The sampled UV light-sheet was directed onto a fluorescent acrylic plate (FSK2, Thorlabs). The generated emission was imaged by

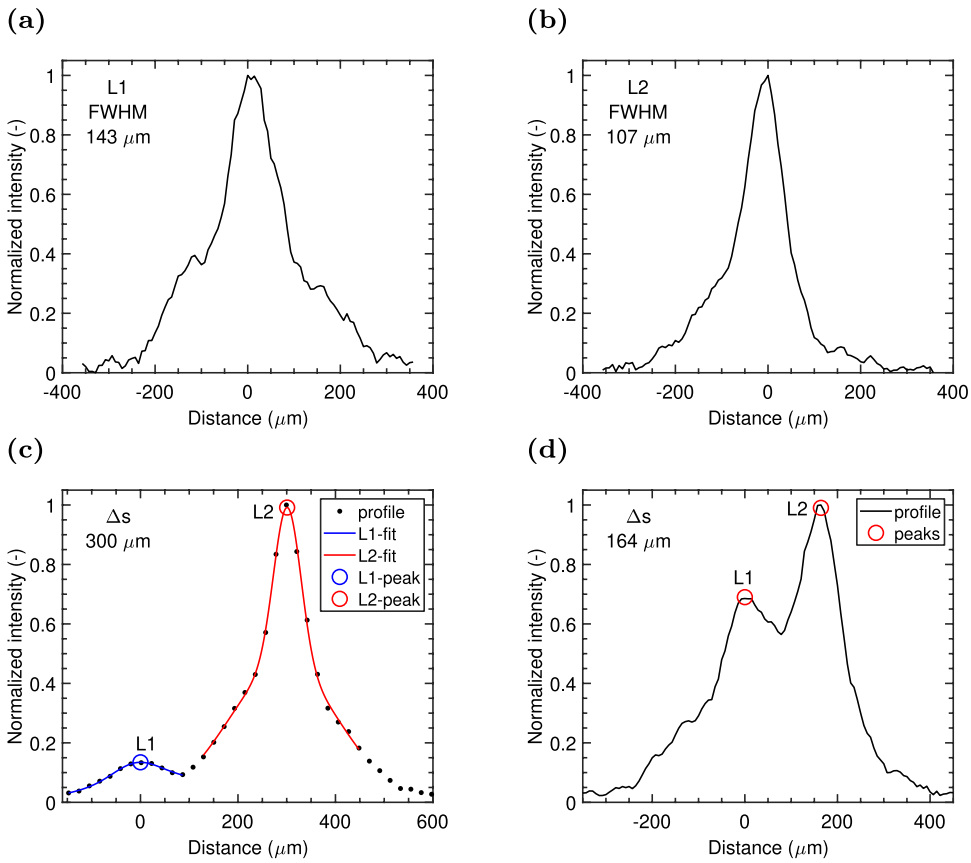

Fig. 2 Laser sheet characterization: **a** L1 sheet with FWHM value, **b** L2 sheet with FWHM value, **c** L1 and L2 separated by 300 µm, and **d** L1 and L2 separated by 164 µm

the C3 CCD camera (Imager Intense, LaVision). To avoid camera saturation, a delay of 67 µs was used relative to the first laser pulse while the camera exposure was set to 100 µs for the mean $\Delta s = 304$ µm dataset. For the mean $\Delta s = 109$ µm dataset, the delay value was optimized to 52 µs while maintaining 100 µs exposure. The presence of an emission signal with such a long delay is probably due to phosphorescence. Acrylic polymers can have a long phosphorescence lifetime, as noted in Unterleitner and Hormats (1965). The C3 camera was equipped with a visible-spectrum lens (50 mm f# 1.4, AF Nikkor, Nikkon) that blocks excitation UV light. Spacers were used to achieve the desired digital resolution in the range of 47 (for mean $\Delta s = 304$ µm) to 140 (for mean $\Delta s = 109$ µm) pixels/mm. This scaling is sufficient to resolve Δs. Depending upon the requirement, Δs can be varied from 50 to 350 µm.

To determine the sheet thickness, each laser sheet was imaged independently. Figure 2a and b shows the L1 and L2 laser-sheet profiles derived from a single-shot/instantaneous image. The laser pulse energy of L1 and L2 was 9 mJ and 36 mJ, respectively. To deduce these profiles, an image was acquired at 140 pixels/mm digital resolution. For improving the SNR, data was vertically averaged over a 0.3 mm height. The full width at half maximum (FWHM) was used to characterize the sheet thickness. For L1, FWHM was 143 µm, while for L2, the FWHM value was 107 µm. Figure 2c and d shows L1 and L2 sheets together (temporally separated by 800 ns) along with the corresponding Δs value. For $\Delta s = 300$ µm, spatial discretization was 47 pixels/mm. For improving the SNR, data was vertically averaged over a 3.2 mm height. The average laser energy was 5 mJ and 40 mJ for L1 and L2, respectively. This energy ratio is approximately reflected in Fig. 2c. For such separation distance, L1 and L2 sheets are reasonably separated with minimal overlap. The peak of the light-sheet profile was determined by fitting a Gaussian distribution to the data. Thus, Δs can be located within a sub-pixel range.

For $\Delta s = 164$ µm (Fig. 2d), there was an appreciable overlap between laser sheets. Nonetheless, peaks can be discerned without any difficulty. This data was acquired with 140 pixels/mm discretization. In order to improve the SNR, data was vertically averaged over a 0.3 mm height. Unlike 47 pixels/mm data, for 140 pixels/mm data, peaks were identified without fitting any curve, as the spatial discretization was sufficient. The laser energy was 9 mJ and 36 mJ for L1 and L2, respectively. To maintain comparable signal intensity across L1 and L2 sheets, the bottom region of the light-sheet was imaged. Since both light-sheet heights were not identical (due to minor differences in beam diameters), the proportionate signal was not observed in Fig. 2d, unlike Fig. 2c where a nearly central region of the light-sheet was imaged.

2.2.2 Imaging cameras

The acetone-PLIF signal in the visible spectrum was collected normal to the light-sheet using a CCD camera (Imager Intense, LaVision). An intensified CCD camera was not preferred since it can lead to higher photon shot noise, as indicated earlier. All three cameras, C1, C2, and C3 (indicated in Fig. 1), were identical with a resolution of 1376×1040 pixels. To enhance the SNR, hardware binning of factor two was incorporated. Thus, the effective resolution was reduced to 688×520 pixels. The signal was imaged through a visible-spectrum imaging lens. Since this lens blocks UV wavelengths, no separate filter was needed to block the excitation wavelength (266 nm). For the C1 camera, a 58 mm f/2.8 (Sigma) lens was used. For the C2 camera, a 105 mm f/2 (AF-DC Nikkor, Nikon) lens was used. To reach the desired magnification, spacers were used between the lens and camera. The digital resolution for both cameras was around 20.5 pixels/mm. Note that the optical resolution differs from the digital resolution. We characterized the optical resolution by imaging a sharp line printed on a transparent sheet. A traversing knife-edge approach could have been used for better accuracy. Due to limited resolution, the edge/step response function (SRF) deteriorates, and this signature can provide an estimate of the resolution. The spatial derivative of SRF provides a line spread function (LSF). In this deduction, to minimize the noise influence, data were fitted with appropriate functions. The fitted curves were used for further processing. SRF was fitted with a sigmoid function which is close to the error function. LSF was fitted with a Gaussian function. For the Gaussian LSF assumption, resolution can be defined by the standard deviation (σ_{LSF}), similar to Kaiser and Frank (2011). The estimated optical resolutions, σ_{LSF}, for the C1 and C2 cameras were 78 µm and 62 µm, respectively. This resolution is comparable to the light-sheet thickness. By assuming a Gaussian beam profile, the standard deviation thickness of a light-sheet (σ_{LS}) can be obtained from FWHM. For L1 and L2 laser-sheets, σ_{LS} is 61 µm and 45 µm, respectively. These values are comparable to the Batchelor scale ($56 - 62$ µm estimated subsequently). The imaged field-of-view (FOV) was 31 mm × 25 mm. To evaluate the out-of-plane gradient, PLIF images from both planes need to be perfectly aligned. FOVs of C1 and C2 cameras (i.e., I1 and I2 images, respectively) were spatially aligned within a few pixels during the data acquisition. Next, a pixel-by-pixel mapping across I1 and I2 was achieved by applying a second-degree polynomial transformation using a calibration target printed on a transparent sheet. This procedure ensured the overlap of I1 and I2 images within a pixel (~50 µm). The I1 image was used as a reference. For the transformed I2 image, the deduced optical resolution was $\sigma_{LSF} = 79$ µm, nearly the same as of I1. The in-plane gradients of SDR

were evaluated from the transformed I2 image. The I1 and I2 images were used for obtaining the out-of-plane scalar gradient.

2.2.3 Laser fluence

The linearity of the acetone-PLIF signal with laser energy was verified. The acetone-PLIF signal in a potential core of the laminar jet was measured as a function of the laser energy. The laser energy was controlled by a beam attenuator which consisted of a half-wave plate and a polarizer. The use of an attenuator facilitated energy variation at a constant laser pulse width (~6 ns). The PLIF signal was confirmed to be nearly linear until 40 mJ energy. A mild non-linearity was noted between the 40–76 mJ energy range. Beyond 76 mJ energy, the PLIF signal saturated and even reduced mildly. The reduction in PLIF signal is likely attributed to the photodissociation of acetone which can occur at higher laser fluence. Therefore, we restricted the laser energy to 40 mJ, which translates to the corresponding fluence of 0.6 J/cm^2.

Note that our above-stated fluence characterization is valid only for a pulse repetition rate of 10 Hz. It has been shown that at a higher pulse repetition rate, acetone tends to dissociate even at a lower fluence (Papageorge and Sutton 2017). For dual-plane PLIF, we used two successive laser pulses separated temporally by 800 ns. Although light-sheet peaks were spatially separated, low-intensity regions of the light-sheet overlapped in space, as observed from Fig. 2c. This overlap increased with a reduction in sheet separation distance, as observed from Fig. 2d. Due to such overlap, there was a possibility of photodissociation. To confirm this, we compared successive PLIF images. Recall that PLIF images acquired from L1/C1 and L2/C2 systems are denoted as I1 and I2, respectively. The first laser pulse corresponds to L1. The subsequent laser pulse (L2) was delivered after 800 ns relative to L1.

In the I1 image, no artifacts were noted even at a moderate pulse energy of 40 mJ, conforming to the previously mentioned linear-LIF regime. However, the use of energy beyond 10 mJ of L1 resulted in artifacts in the second image I2. In I2, we noted a region of lower (relative to I1) PLIF signal. This is attributed to the photodissociation created by the L1 pulse. The PLIF image from the first L1 plane did not show any such artifact since the laser pulse is only ~6 ns long. Acetone dissociation timescales are expected to be longer than the laser pulse width and associated fluorescence lifetime. The dissociation effect becomes apparent in the I2 PLIF image, which was acquired after 800 ns relative to L1. This implies that the photodissociation effect exists even below 40 mJ energy (within the linear PLIF regime); however, this effect is not captured since the PLIF signal timescale is only a few ns. At substantially higher laser energy (e.g., > 76 mJ), the rate of photodissociation may match the LIF timescale. Consequently, the LIF signal reduction effect is reflected *instantaneously* at high laser energy. To minimize the dissociation-induced artifacts in the I2 image, the laser energy of L1 was reduced. It was found that below 10 mJ energy of L1, there were no apparent artifacts in the I2 image. The use of higher energy (up to 70 mJ) for the L2 did not show any artifacts on the corresponding I2 image. Consequently, we chose to use the energy of 5 mJ for L1 and 40 mJ for L2 for the data acquired at a mean Δs of 304 µm. These energy values were further optimized for the mean $\Delta s = 109$ µm dataset, where 9 mJ was used for L1 (to improve the SNR) and 36 mJ for L2. Such variation of laser energy did not affect the deduced SDR appreciably, as evidenced by the comparison of mean 2D SDR fields (detailed in Sect. 3.1.1).

2.3 Image corrections

Quantification of mole fraction from the acetone-PLIF signal requires a series of image corrections. Raw PLIF images are corrected for background noise, laser-sheet energy profile, and laser-sheet extinction. Figure 3a shows the instantaneous raw PLIF image (from the C1 camera) acquired in a laminar jet of air. The acetone-seeded air was passed through the central tube. The air flow rate through the acetone bubbler was 5 lpm. As indicated in Sect. 2.1, the estimated acetone concentration was 37%. Thus, the acetone-air mixture flow rate was 6.85 lpm. The background signal was acquired without any flow but with the laser switched on. The laser-sheet (LS) profile was acquired in a potential core of the

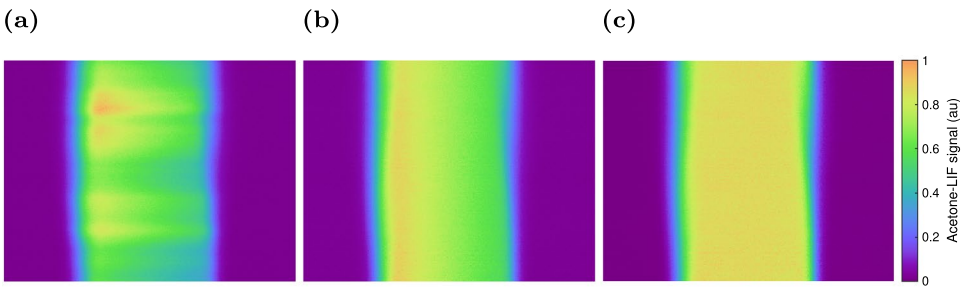

Fig. 3 An illustration of PLIF image correction in a laminar jet: **a** raw image, **b** light-sheet profile corrected image, **c** extinction corrected image. The images are 31 mm × 25 mm in size

present laminar jet. Acetone concentration within the potential core is assumed to be constant. The LS corrected image is shown in Fig. 3b. This correction partially accounts for flat-field correction. Since only a single 1D profile is considered, field-wide system response in the horizontal direction is not accounted for. Since SDR is a small-scale quantity with sharp gradients in a narrow region, the error associated with the partial flat-field correction is expected to be negligible. The laser energy decreases exponentially in the propagation direction due to photon absorption by acetone molecules. Within the potential core of the jet, we obtain this exponential decay, and the same is used to incorporate an approximate extinction correction. The corrected image is shown in Fig. 3c.

For the turbulent case, nearly identical image processing steps were used. The images were corrected for the LS profile in two steps. Firstly, the time-averaged LS profile was used. Next, the laser extinction correction was implemented by considering the exponential decay of the LIF signal in the direction of laser propagation. Next, to account for shot-to-shot fluctuation of the laser-sheet profile, instantaneous LS correction was incorporated. Due to low swirl intensity, unmixed regions of the jet were available throughout the imaged axial distance. The LIF signal intensity in the unmixed region at each axial pixel location was radially averaged, from which a residual LS profile correction was performed. Finally, the arbitrary camera counts were converted to the jet mole fraction by assuming $X_f = 1$ in the potential core of the jet. The spatially averaged value in a 1.5 mm square region, centered at 11 mm above the jet exit (along the axis), was selected to assign $X_f = 1$. Such spatial averaging enhances the reliability of X_f instead of considering the maximum value which is affected by the noise. This normalization was performed on an instantaneous basis. Consequently, any shot-to-shot variations of laser energy and sheet profile have been accounted for. The background signal was subtracted based on a spatially averaged value by assuming $X_f = 0$ away from the jet where no mixing is expected. Though we incorporate time-averaged background subtraction, a minute time-variation of background signal is possible in CCD cameras. Thus, spatially averaged value in a 0.5 mm square region, centered at $(r, z) = (16.5, 10.5)$ mm, was selected to assign $X_f = 0$ in each image.

3 Results and discussion

3.1 In-plane 2D SDR

In this section, in-plane two-component SDR is presented along with a discussion on various aspects that can affect the SDR accuracy. In the following subsection, the influence of noise on SDR is presented along with details of the Wiener filtering method. A systematic bias in SDR is assessed by comparing 2D SDR from I1 and I2 datasets at different laser energies. The subsequent section deals with the resolution assessment. Both the in-plane and out-of-plane resolutions are discussed. The resolution requirement is deduced from the dissipation spectrum using the Bachelor scale estimate. Through the noise and resolution analysis, uncertainty in 2D SDR is assessed in the last subsection. The full three-component SDR deduction is discussed subsequently (Sect. 3.2.1).

3.1.1 Noise filtering

As indicated in the Introduction, the evaluation of SDR is difficult due to noise and limited spatial resolution. We first demonstrate the influence of noise. Figure 4a shows the background, light-sheet, and extinction corrected jet concentration field for the considered turbulent swirl flow. In principle, values of X_f should lie in the range of 0 to 1. However, values outside this range are apparent in Fig. 4a due to noise. The signal intensity fluctuates from pixel to pixel; however, area-averaged values of X_f in the potential core are close to the expected value (i.e., 1). To quantify the extent of noise, the SNR is deduced from the mean (μ) and standard deviation (σ) of signal intensity within a potential core region. The value of SNR (μ/σ) for an unfiltered image is ≈ 18 for an I1 (from the C1 camera) image acquired at 5 mJ mean laser energy. At 9 mJ mean energy, the SNR of I1 improved to ≈ 23. For the I2 image (from the C2 camera) acquired at 40 mJ laser energy, the corresponding SNR is ≈ 29. Recall, for I2 acquisition, the energy between two campaigns did not vary appreciably (36–40 mJ).

Figure 4b shows the two-component SDR, χ_{2C}, evaluated from the unfiltered X_f image. To evaluate SDR, it is convenient to use the Cartesian coordinates, where unit vectors x_1, x_2, and x_3 are aligned to r, z, and azimuthal (normal to the imaging plane) directions, respectively. Let, conserved scalar ζ be X_f. Then, SDR can be expressed as,

$$\chi = 2D\left[\left(\frac{\partial\zeta}{\partial x_1}\right)^2 + \left(\frac{\partial\zeta}{\partial x_2}\right)^2 + \left(\frac{\partial\zeta}{\partial x_3}\right)^2\right] \tag{1}$$

From a planar image, gradients only in x_1 and x_2 directions are accessible. Therefore, two-component SDR is expressed as,

$$\chi_{2C} = 2D\left[\left(\frac{\partial\zeta}{\partial x_1}\right)^2 + \left(\frac{\partial\zeta}{\partial x_2}\right)^2\right] \tag{2}$$

The gradients are obtained through the central difference method. In the potential core of the jet, χ_{2C} should be negligible since no spatial variation of X_f is expected. However, in Fig. 4b appreciable values of χ_{2C} are observed

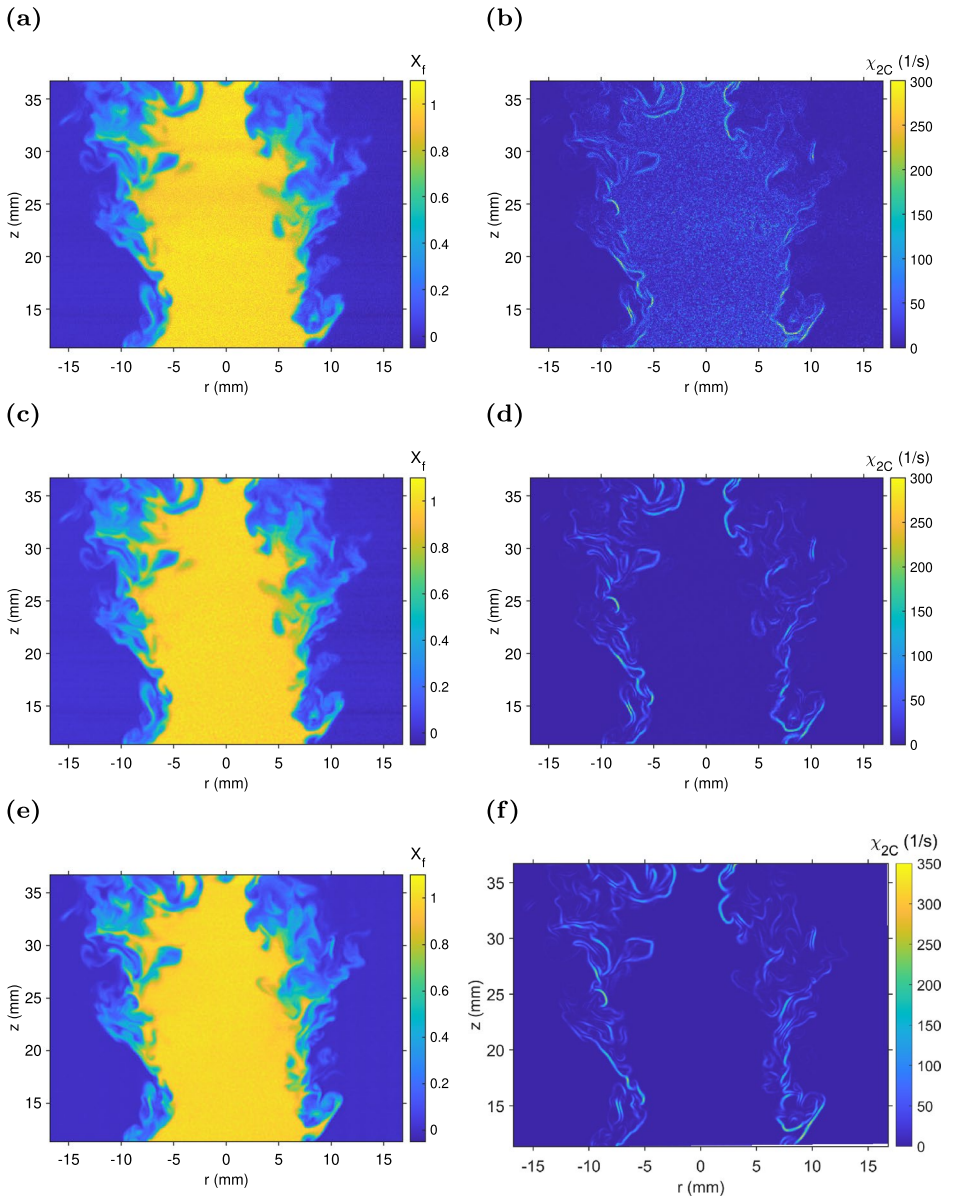

Fig. 4 SDR demonstration in the turbulent swirl flow at $\Delta s = 338$ μm: **a** Unfiltered jet mole fraction, **b** SDR from an unfiltered image, **c** Filtered mole fraction from I1, **d** SDR from filtered I1 image, **e** Filtered mole fraction from I2, and **f** SDR from filtered I2 image. z axis begins from the exit plane of the inner tube as shown in Fig. 1

due to noise. To mitigate this issue, a special Wiener filtering is performed on the X_f image as detailed in Refs. Soulopoulos et al. (2014) and Stetsyuk et al. (2016). The procedure is briefly summarized here. A 2D scalar energy spectrum is evaluated for each instantaneous image. A discrete/fast Fourier transform (FFT) of the fluctuating component of the mole fraction ($\zeta' = \zeta - \langle\zeta\rangle$) is evaluated. The square of the FFT term provides PSD of scalar energy (see, for instance, Wang et al. (2007, 2007a)). 2D FFT fields are averaged over the number of images to provide the ensemble-averaged energy spectrum. Next, a profile in a radial direction of the wavenumber space is extracted to obtain a 1D radial energy spectrum (presented subsequently in Fig. 6). This radial spectrum provides an estimate of the noise in the wavenumber space. At large flow scales (i.e., low wavenumbers), the spectrum is nearly noise-free. On the other hand, the energy spectrum at small scales (high wavenumber) is substantially noisy. The spectrum decreases with wavenumber and eventually reaches a plateau due to noise which is referred to as a noise-floor (Wang et al. 2007, 2007a).

Based on a general trend of the PSD, behavior for the noisy part of the PSD (from a certain cut-off wavenumber) can be modeled (or extrapolated) by an exponential function. Besides the noise correction, the Wiener filter also accounts for image blurring. A point spread function (PSF) is used to quantify the image blur caused by the limited optical resolution. The camera response to a sharp edge (i.e., step) of the printed line is used to obtain the line spread function (LSF) as indicated earlier in Sect. 2.2.2. For the

Gaussian shape, LSF can be approximated to PSF (Smith 1997). This PSF information is included while designing the Wiener filter to account for a limited optical resolution. Further details of this intricate procedure are elucidated in Soulopoulos et al. (2014). The cut-off length scale for the modeled part of the PSD is 0.5 mm in the present work.

Figure 4c shows the Wiener-filtered image, which exhibits the SNR of ≈ 80. This is a substantial enhancement relative to an unfiltered image (where the SNR was around 18). Due to reduced noise, X_f approaches the expected range of 0 to 1. χ_{2C} evaluated from the filtered image is shown in Fig. 4d which shows significant enhancement. χ_{2C} values in the jet core are negligible, as expected. Additionally, SDR layers appear smooth relative to Fig. 4b. Besides the I1 (from C1/L1) image, we also evaluate 2D SDR from I2 (from C2/L2) image acquired in the adjacent plane with $\Delta s = 338$ µm. Figure 4e shows the filtered image from I2 data, which exhibits the SNR of ≈ 94. The SNR is more due to the higher laser energy of L2. χ_{2C} from I1 and I2 (Fig. 4f) are remarkably similar in distribution and in intensity. SDR values appear higher in the I2 data. The peak χ_{2C} in I1 data is 245 s^{-1}, while it is about 310 s^{-1} for I2. There are mild differences in the SDR-layer shapes. Note, SDR from I1 and I2 are not expected to be identical since Δs is larger than the smallest mixing length scale (that is estimated subsequently). Nonetheless, to assess systematic biases between two independent PLIF systems, we compared mean χ_{2C} fields deduced from I1 and I2 datasets. In I2, due to the use of higher laser energy (that led to better SNR), SDR values were mildly higher. To quantify the difference, we evaluated the spatial average over the entire FOV. The area-averaged SDR values for I1 (at 5 mJ) and I2 (at 40 mJ) are in agreement within ±2%. Although, local differences at a few locations are as high as ±13%. The agreement between I1 and I2 improves when L1 laser energy is increased. The mean SDR for the I1 (at 9 mJ) and I2 (at 36 mJ) dataset is presented in the Appendix (Fig. 17), which shows nearly identical SDR fields between two PLIF systems. The highest difference between local SDR is reduced to ±11%, which is within the estimated uncertainty (see Sect. 3.1.3).

Peak χ_{2C} values are around 250 to 300 s^{-1}. We compare this magnitude with the past χ_{2C} reported at approximately identical condition ($S = 0.3$ and Re = 27000). The present χ_{2C} is one order of magnitude greater than reported in Stetsyuk et al. (2016). Likely reasons for this discrepancy are discussed next. There are a few differences in the optical setup and flow instrumentation. In Stetsyuk et al. (2016), pre-calibrated rotameters were used for flow metering, while the present work uses thermal mass flow controllers which provide superior accuracy over the former. Nonetheless, if flows are sufficiently turbulent, differences in flow conditions should not alter SDR by an order of magnitude. There are two key differences in the optical setup, namely resolution and laser fluence. In Stetsyuk et al. (2016), the resolution was estimated to be 350 µm at 50% of the peak MTF (obtained using a slanted-edge technique). In the present case, the corresponding resolution value (at 50% of peak MTF) is estimated to be 200 µm for C1 and transformed C2 images. This difference in resolution may lead to an appreciable reduction in SDR in Stetsyuk et al. (2016). Although the limited optical resolution is accounted for through PSF during Wiener filtering, there exists uncertainty in the PSF measurements in both the present and Stetsyuk et al. (2016) experiments. Furthermore, in Stetsyuk et al. (2016), a 50 mm focal length imaging lens was used at an f-number of 1.4. Due to the smaller f-number, there is a possibility of image de-focusing. We used f-number between 2 to 2.8. Despite the finite optical resolution correction, errors can occur due to uncertainty in MTF measurement and also due to lens de-focusing. Next, we discuss the influence of laser fluence which was appreciably higher (estimated to be 4 J/cm^2) in Stetsyuk et al. (2016). Such high fluence can dissociate acetone, as verified in the present work (up to 1.5 J/cm^2). If dissociation occurs to the same extent throughout the imaged field, then the impact on SDR would be lower. Note that the local fluence can change due to the variation of laser-sheet thickness along the width of the FOV. In Stetsyuk et al. (2016), laser-sheet was formed using a single cylindrical lens of $f = 310$ mm. Such a short focal length alters the fluence spatially. The variation of fluence in a non-linear regime (especially with photodissociation) may skew the acetone-PLIF profile, which in turn affects SDR deduction. Therefore, it is advised to perform quantitative acetone-PLIF measurements at low laser fluence. In summary, the SDR differences between the present and Stetsyuk et al. (2016) measurements could primarily be attributed to low resolution and high laser fluence used in the past, with a minor contribution from the difference in flow condition. Diffusivity value in Stetsyuk et al. (2016) was taken as 0.124 cm^2/s, while in the present work it is 0.1 cm^2/s based on the correlation (Yaws 2009) and assumed gas temperature of 20 °C. For identical diffusivity, differences in SDR would further be higher.

3.1.2 Resolution assessment

A limited resolution could underestimate the SDR value. Note that the effect of a finite light-sheet thickness on SDR is demonstrated (Kaiser and Frank 2011) to be of lesser concern up to a certain sheet thickness. Instead, the in-plane resolution, where differentiation is performed, plays a primary role. The in-plane and out-of-plane resolution contributions to SDR are matched when the laser-sheet thickness is approximately four times the in-plane resolution (Kaiser and Frank 2011). As indicated earlier, the present in-plane resolution, σ_{LSF} is 62 − 78 µm and light-sheet

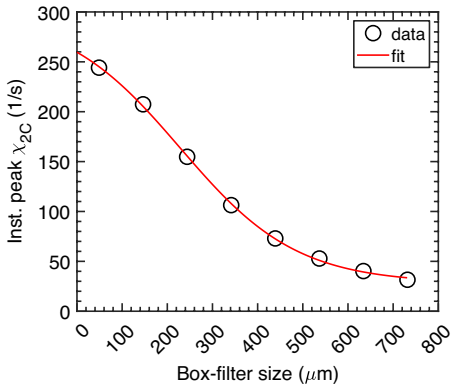

Fig. 5 Effect of spatial resolution on instantaneous peak SDR

thickness, σ_{LS} is $45-61$ µm. Thus, the influence of finite sheet thickness (out-of-plane resolution) on SDR is expected to be significantly lower than the in-plane resolution effect. As indicated earlier, we accounted for the finite in-plane optical resolution through PSF in the Wiener filtering process.

Due to hardware binning, camera digital resolution is reduced to 50 µm/*pixel*. This finite digital resolution spatially averages any X_f differences occurring within 50 µm pixel resolution. To estimate the impact of this pixel resolution, we successively degrade images, similar to (Barlow and Karpetis 2005; Wang and Barlow 2007). The resolution of a Wiener-filtered X_f image (e.g., Fig. 4c) is degraded by using a Box filter. Though the resolution is degraded, the sampling frequency (i.e., spacing or number of pixels) remains the same. SDR is deduced for Box-filtered images with different box sizes. A peak SDR intensity (in a given FOV) is used as a representative value. Figure 5 shows the effect of a Box filter size. The overall trend of this resolution curve is quite similar to the analysis of Wang and Barlow (2007). To extrapolate the SDR value at a zero filter width, we fit a Sigmoid function to the data. Based on the extrapolated value, the finite resolution of the present data is expected to negatively bias the SDR only by ~6%. Besides the experimental data, we also examined the influence of the filtering analytically using the model spectrum similar to Wang et al. (2007b). This analysis is included in Appendix 1 for the present λ_B and assumed Re_λ. For the resolution of 50 µm, the SDR accuracy of better than 1% can be achieved in the absence of noise. Thus, the present resolution appears to be sufficient to resolve the finer mixing length scales.

The smallest mixing length scale is described by the Batchelor scale, λ_B. In the past, a strain-limited diffusive length scale (λ_D) has been used to determine the resolution requirement. However, depending upon the gradient stencil, the resolution requirement can approach λ_B (discussed subsequently in Sect. 3.1.3). Consequently, accurate estimation of even in-plane SDR (χ_{2C}) is extremely difficult, especially at higher Re, as of the present case. It is also difficult to estimate λ_B *apriori* for the present swirling flow. For simple configurations such as round or planar jets, λ_B and Reynolds number correlations (Antonia et al. 1980; Mi and Nathan 2003) are available for fully developed regions of the flow. Since the present configuration differs from a jet (due to swirl and near-field developing region), correlations reported previously could not be used for obtaining λ_B. Therefore, an alternative approach based on the dissipation spectrum is used to obtain λ_B. Wang et al. (2007) demonstrated that λ_B could be linked to a wavenumber where the power of dissipation spectrum measures 2% of the peak value. This approach is relatively robust and can be applied to a range of turbulent flows, e.g., reacting, developing, or swirling flows. Therefore, several studies (Frank and Kaiser 2007; Petersen and Ghandhi 2011; Kaiser and Frank 2011; Soulopoulos et al. 2014; Stetsyuk et al. 2016) have deduced λ_B from the dissipation spectrum. Note that the portion of the scalar dissipation spectrum where power drops to 2% of the peak needs to be sufficiently noise-free. Our present PSD data satisfies this requirement thanks to the Wiener-filtering strategy. We evaluate λ_B from

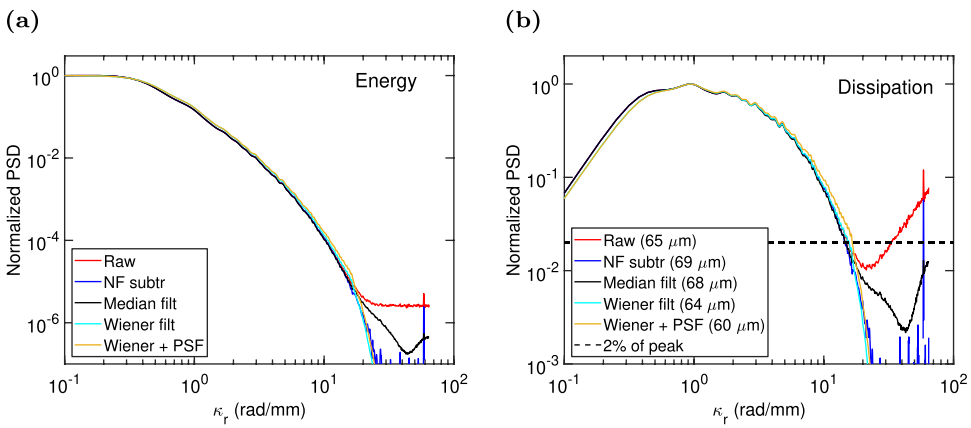

Fig. 6 Mean radial spectrum of fluctuating scalar, ζ', **a** energy and **b** dissipation. The Bachelor scale is indicated for each PSD curve. The data is from I2 image set with laser energy of 40 mJ

a radial profile of the 2D spectrum. The energy spectrum is evaluated for the fluctuating component of the scalar (ζ'), following Wang et al. (2007a). An ensemble-averaged 2D PSD field is obtained, from which a radial PSD profile is extracted similar to Soulopoulos et al. (2014). From this energy spectrum profile, a dissipation spectrum is obtained similar to Wang et al. (2007a). Such 1D PSD profiles of energy and dissipation are shown in Fig. 6. Besides the raw (unfiltered) spectrum, filtered spectra are also deduced. Different filtering approaches were compared to assess the effectiveness of the implemented Wiener filter. Ordinary median (kernel size 3 pixels) filtered ζ' fields are used to reduce noise. A noise-floor (NF) subtraction-based spectrum is also deduced following Renfro et al. (2000). The noise-floor cut-off wavenumber is identified where the raw dissipation spectrum measures minimum. The energy spectrum beyond this wavenumber is dominated by noise. Thus, the average magnitude value of the noisy part of the spectrum is subtracted from the raw energy spectrum. The spectrum of Wiener filtered data with and without point spread function correction is also examined. For each of these spectra, λ_B is evaluated as a scale where dissipation spectrum magnitude reaches 2% of the peak value.

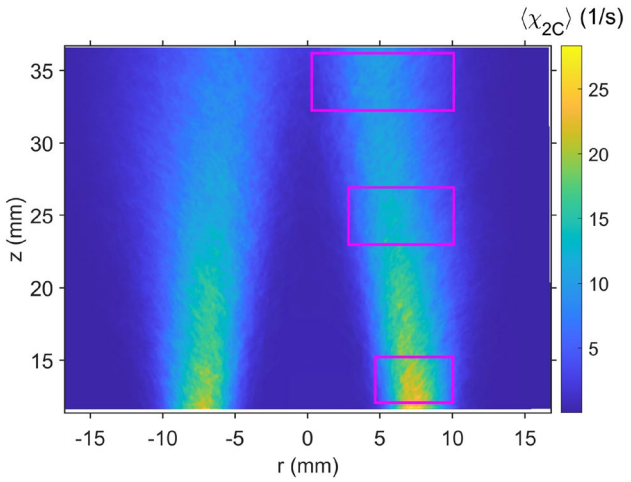

Fig. 7 Bottom, mid, and top regions of interest marked on the mean 2D SDR field

As the spectrum is evaluated for the entire imaged field (as in Fig. 4c), the calculated λ_B is the global estimate for a given FOV. Since the data is acquired in two planes (corresponding to I1 and I2 images), two independent estimates of λ_B can be obtained. λ_B from I1 and I2 lies in the range of 58– 60 µm. Owing to a better SNR, PSDs from the I2 image set (at 40 mJ laser energy) are shown in Fig. 6.

Overall, there is a good agreement between NF-filtered PSD and Wiener-filtered PSD. The inclusion of PSF provides a mildly distinct PSD form. Next, the Bachelor

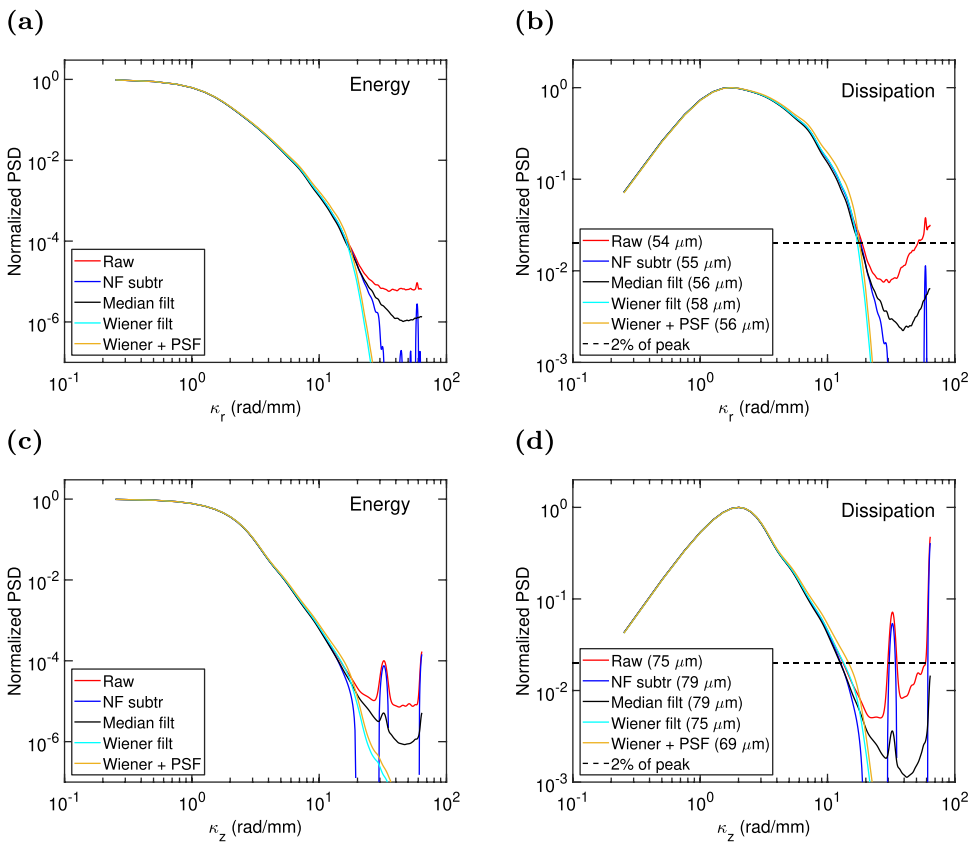

Fig. 8 Mean spectrum of fluctuating scalar, ζ', for the bottom ROI **a** radial energy, **b** radial dissipation, **c** axial energy, **d** axial dissipation. The Bachelor scale is indicated for each PSD curve

scale from each of the PSD curves is compared. Due to a better SNR of the I2 set, even the raw spectrum appears to provide a close estimate of the Bachelor scale. λ_B increases with noise filtering. For NF-filtered and Median-filtered data, λ_B is almost the same. Wiener-filtered PSD provides nearly the same λ_B as the raw PSD. Wiener- and PSF-filtered PSD provides a smaller λ_B since PSF compensates for the limited optical resolution. Therefore, for the overall field, λ_B is taken to be 60 µm.

Since the Bachelor scale varies with downstream distance, we also evaluate the regional PSDs. As shown in Fig. 7, three regions around the shear layer are considered. For bottom, mid, and top regions of interest (ROIs), (r, z) ranges are (4.7–10, 12–15.2), (2.8–10.1, 23–26.9), (0.3–10.1, 32.2–36.2) mm, respectively. For each ROI, both the axial and radial PSDs are evaluated. Similar to Fig. 6, data from I2 image set (at 40 mJ) is used to obtain PSDs.

Similar to the previous analysis, PSDs from different filtering methods are included in Fig. 8 for the bottom ROI. Unlike Fig. 6, there are differences in PSDs at high wavenumber. This is due to the global correction nature of the designed Wiener filter. The present Wiener filter is based on the radial energy spectrum of the entire imaged field. For regional PSDs, λ_B based on PSF correction and Wiener filtering is taken as a relevant scale for further discussion. As expected, λ_B obtained from the radial spectrum is smaller than its axial counterpart. The regional radial λ_B (56 µm) is mildly lower than the earlier global estimate of 60 µm. For the axial spectrum, in the noise-dominated region, a distinct peak is observed owing to the interline-transfer CCD camera that can produce discontinuity of the signal between pixel rows. This noise reduces with the median filtering, whereas the application of the Wiener filter removes this noise peak entirely.

For mid and top ROIs, radial and axial spectra are included in the appendix (Figs. 19 and 20). The agreement between different filtering methods improves with axial distance. Within the shear layer, λ_B based on the radial spectrum increases from 56 to 62 µm with axial distance. As expected, λ_B obtained from the axial spectrum measures higher, ranging from 69 to 99 µm. Even the raw spectrum is reasonably resolved to provide the Bachelor scale estimate. The raw spectrum is free from systematic biases that may arise through the filtering process. λ_B deduced from the raw radial spectrum varies from 54 to 69 µm, whereas its axial counterpart varies from 75 to 102 µm.

Based on this analysis, the resolution requirement is determined to be 56 µm for the present flow, which is very stringent for optical techniques. Note, though the measured optical resolution is lower ($\sigma_{LSF} = 78 - 79$ µm), we account for it through PSF correction during Wiener filtering. The resolution curve (Fig. 5) and camera scaling (50 µm/*pixel*) suggest that the present measurement, with associated post-processing, satisfies the resolution requirement for SDR evaluation.

3.1.3 Uncertainty in 2D SDR

SDR measurement is primarily affected by biases resulting from a limited SNR, noise filtering effects, and finite resolution. The uncertainty in the X_f field is mainly caused by the photon shot noise. Based on SNR, the uncertainty in a filtered X_f is estimated to be ±2.5% with a 95% confidence interval (CI). Consequently, the uncertainty in SDR is estimated to be ±10% through a sensitivity analysis. Note that this estimate only accounts for a finite SNR. The uncertainty from a sub-optimal Wiener filter is assessed by varying the cut-off wavenumber beyond which the spectrum is modeled with an exponential fit. A reduction in cut-off wavenumber from 2 to 1.43 mm^{-1} reduces the peak instantaneous SDR by 23%. For a given cut-off wavenumber (2 mm^{-1}), there is an excellent agreement in the mean SDR fields across two PLIF systems, as observed from Fig. 17. Nevertheless, based on the differences between the Bachelor scales evaluated from different filtering approaches, the filtering uncertainty is approximated to be ±10%.

The use of a central difference scheme (to evaluate gradient) leads to artificial filtering, which could reduce SDR. To assess the extent of SDR reduction, we compare the SDR obtained through central difference with that of two-point (forward/backward) difference. SDR with the central difference is under-predicted by ≈ 6% relative to a two-point difference. Such a small influence is due to the reduction in noise through Wiener filtering. For the ordinary median filtered field, variation in central and two-point differenced SDR is as high as ≈ 40%. Since the error for Wiener filtered data is not significant, we retain the central difference approach in favour of its lower sensitivity to noise. The influence of numerical stencil (used to obtain gradient) on SDR has been analyzed by Wang et al. (2007b). For central difference stencil, over-resolved data is needed to minimize the errors in SDR. To resolve the dissipation spectrum up to the characteristic cut-off scale of $2\pi\lambda_B$, the minimum resolution needs to be $\pi\lambda_B$ (Wang et al. 2007). If the optical blurring effects are accounted for through the point spread function, then the effective resolution is determined by the sampling frequency. For the present data, the sampling resolution is 50 µm. Thus, data appears to be over-resolved by a factor of 3.5 considering the lower estimate of $\lambda_B = 56$ µm. The closer agreement (within 6%) between the two-point and centrally differenced SDR values confirms the over-resolution of the present data, based on the results of Wang et al. (2007b).

By considering errors in X_f, Wiener filtering, finite resolution (Fig. 5), and central difference filtering, the combined uncertainty in an instantaneous χ_{2C} is estimated

to be ±17%. Note that since this value is deduced by considering various measurement biases, it is a relative estimate of uncertainty. Due to the complexity of swirling flow in the developing region, the absolute estimate of uncertainty could not be obtained. For simple configurations, such as planar or round jets, a reference SDR value could be obtained from previous measurements.

3.2 SDR components

The discussion in the earlier section is focused on in-plane two-component SDR and associated measurement biases. The present section examines the influence of laser-sheet separation distance on the out-of-plane SDR component.

3.2.1 Out-of-plane SDR component

The full three-component SDR requires a scalar gradient in the third direction as well, as indicated by Eq. 1. We define the SDR components as, $\chi_i = 2D(\partial\zeta/\partial x_i)^2$. Consequently, χ_1, χ_2, and χ_3 are the SDR components in x_1, x_2, and x_3 directions, respectively. x_1, x_2, and x_3 are radial, axial, and azimuthal directions, respectively, as defined earlier. To obtain the gradient in the x_3 direction, we acquire the mixing field on two planes that are separated by distance Δs, as illustrated in Fig. 1. In the past (Buch and Dahm 1998; Su and Clemens 1999), Δs requirement had been determined based on λ_D rather than λ_B. Recall, the in-plane χ_1 and χ_2 components are obtained through central difference, whereas χ_3 is deduced through two-point difference. Consequently, the resolution requirements of in-plane and out-of-plane SDR components are not identical, as discussed earlier. From the previous analysis (Fig. 5), resolution for central difference needs to approach λ_B. For χ_3, due to the two-point difference scheme, the minimum resolution requirement can be larger than λ_B (but $< \pi\lambda_B$). Note, in the absence of noise, over-resolution should not alter χ_3 values. If one applies the in-plane resolution requirement based on λ_B, Δs needs to be 60 µm (global estimate). In this section, we assess the impact of Δs on χ_3.

It is worthwhile to note that, due to several challenges, the accuracy of χ_3 for planar measurements has not yet been rigorously assessed. Although this is a difficult task, we can rely on in-plane components, χ_1 and χ_2. The radial component of SDR (χ_1) is higher than the axial component (χ_2), as expected. This is consistent with the past observations in reacting (Stårner et al. 1994) or non-reacting (Vlad 2021) turbulent jets. In general, axial and radial components are obtained from planar measurements. To obtain the full SDR, isotropy between radial and azimuthal components was assumed in the past (Namazian et al. 1988; Feikema et al. 1996; Stårner et al. 1994). Stårner et al. (1994) relied upon off-axis measurements that indicated anisotropy between radial and azimuthal components to be in the range of 0–20% for a turbulent round jet. Feikema et al. (1996), argued that at a high Reynolds number, instantaneous mixture fraction iso-contours would be highly contorted/wrinkled. Therefore, the normal to a given wrinkled iso-surface will have an equal probability of pointing in radial and azimuthal directions. Thus, isotropy between radial and azimuthal components was assumed. Measurements of Mi et al. (1995) also appear to support the radial-azimuthal isotropy assumption. However, recent DNS results of (Vlad 2021) show that the radial component of mean SDR is stronger than its azimuthal component. Instead, the azimuthal and axial components of SDR are of similar magnitude. Note, most of these previous studies are for the fully developed self-similar region of the round jet, without any swirl. The present measurements are in the developing region of the jet which is surrounded by a swirling coflow of air. Despite this difference, we assume isotropy between axial and azimuthal SDR components based on Vlad (2021). However, the accuracy of azimuthal-axial isotropy was not verified through measurements. An off-axis measurement within the shear layer could have been performed to assess the anisotropy between three components of SDR.

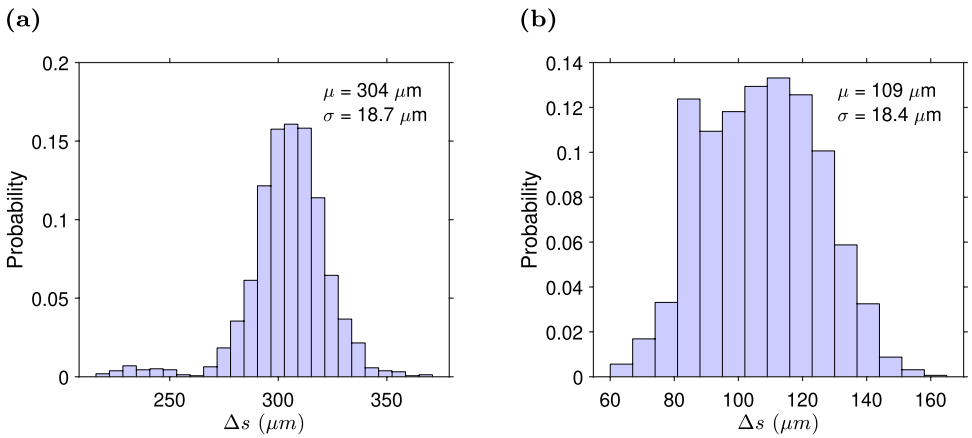

Fig. 9 PDF of laser-sheet separation distance and corresponding standard deviation at mean Δs of **a** 304 µm, and **b** 109 µm

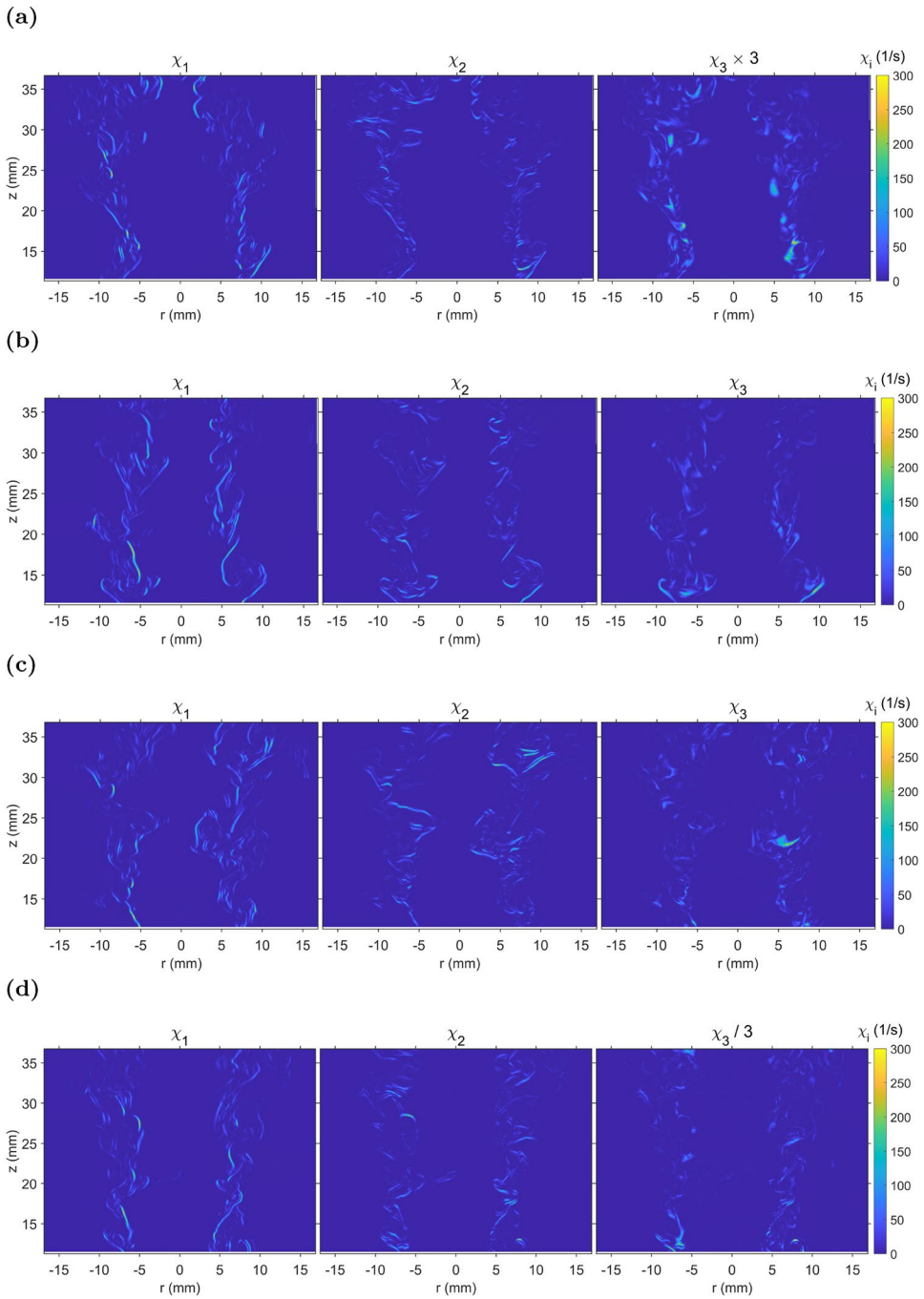

Fig. 10 Effect of laser-sheet spacing on χ_3 component of SDR: **a** $\Delta s = 338$ µm, **b** $\Delta s = 214$ µm, **c** $\Delta s = 114$ µm, and **d** $\Delta s = 64$ µm. Note in (**a**) and (**d**), χ_3 has been scaled for better visibility

Recall that we have access to laser-sheet separation distance, Δs, on a shot-to-shot basis. The data was acquired at mean Δs values of 109 and 304 µm. Figure 9 shows the histogram of Δs variation for each dataset. For the mean 304 µm dataset, instantaneous Δs varies from 215 to 370 µm. For the mean 109 µm dataset, instantaneous Δs varies from 55 to 165 µm. Across both datasets, the standard deviation of Δs (indicated on the PDF) remains nearly identical. Such fluctuation of Δs signifies the need to measure sheet separation distance on a shot-to-shot basis.

Figure 10 shows components of instantaneous χ at different values of Δs. For a preliminary assessment, χ_3 is compared to χ_2. At a larger Δs in Fig. 10a, values of χ_3 are substantially lower than χ_2. Additionally, SDR layers in χ_3 appear more diffused than χ_1 or χ_2. This suggests that $\Delta s = 338$ µm is insufficient to resolve χ_3 structure and intensity. If Δs is reduced to nearly the Batchelor scale at 64 µm, χ_3 values are overestimated, as evident from Fig. 10d. Though the values are overestimated, high-intensity layers of χ_3 generally remain as thin as χ_1 or χ_2. The overestimation

of χ_3 at $\Delta s \approx \lambda_B$ is not surprising. As indicated in the Introduction, from wire-based measurements (Antonia and Mi 1993b) of SDR, $\Delta s < 2\lambda_B$ was observed to produce large values of SDR owing to random and systematic errors, which become dominant at smaller separation distance. In the analytical study (Antonia and Mi 1993a) where measurement noise or systematic error is absent, it has been shown that the smaller separation distance between two parallel wire probes can provide true SDR even at $\Delta s < \lambda_B$. However, in measurements, due to the presence of noise, Δs of $3\lambda_B$ (Danaila et al. 2000) was suggested to provide true SDR for a given wire probe. This estimate of ideal/optimum Δs varies between 1 and $3.33\lambda_B$ across different wire probe-based studies, as reviewed by Antonia and Mi (1993b). The ideal Δs is linked to noise characteristics and systematic biases of a given measurement technique, and the differencing stencil (used to obtain the gradient). The present laser-based measurement differs from wire probes due to the larger thickness of laser sheets (FWHM of $107 - 143$ µm) relative to fine wires. Therefore, it is necessary to analyze the influence of Δs on SDR to identify the optimum separation distance. To obtain χ_3 accurately, two requirements, namely infinitesimally thin laser sheet and infinite SNR, need to be met. These conditions are impossible to satisfy experimentally. We vary Δs between the noise-limited and resolution-limited bounds. Figure 10b and c shows the SDR components with Δs of 214 and 114 µm, respectively. In these figures, χ_3 field is comparable to χ_2. The Δs optimization is further assessed through mean SDR components.

3.2.2 Mean SDR components

Instantaneous images of χ_i provided the preliminary assessment and ideal range of Δs. However, to verify this finding, an analysis based on statistics is necessary to reduce any uncertainty associated with instantaneous fluctuating fields. For isotropic flows, three components of the mean SDR, $\langle \chi_i \rangle$, should be equal, as indicated by Mi et al. (1995) in a turbulent jet. For the present measurements, a high level of anisotropy is noted between radial and axial components of SDR. As discussed in the previous section, based on the DNS data for round jet (Vlad 2021), we assume axial-azimuthal isotropy, i.e., $\langle \chi_2 \rangle = \langle \chi_3 \rangle$. We first obtain the estimate of the in-plane SDR anisotropy. Figure 11 shows $\langle \chi_1 \rangle$, $\langle \chi_2 \rangle$, and $\langle \chi_3 \rangle$ for mean $\Delta s = 304$ µm. A regional anisotropy is deduced as, $K_{12} = \langle \chi_1 \rangle / \langle \chi_2 \rangle$. For this evaluation, only the region where $\langle \chi_1 \rangle$ is greater than 5% of the peak intensity is considered to avoid bias due to negligible values. Anisotropy at three axial zones, namely at the base where $z = 11$ to 15 mm, the mid-region with $z = 20$ to 25 mm, and top zone with $z = 30$ to 35 mm, is evaluated. For a given zone, $\langle \chi_i \rangle$ values are area-averaged to estimate the regional anisotropy. The anisotropy values of K_{12} are 1.55, 1.34, and 1.26 at the base, mid, and top zones, respectively. This indicates that the present flow is highly anisotropic, especially near the jet exit, while anisotropy decreases with downstream distance.

To validate the out-of-plane SDR component, we assume $\langle \chi_2 \rangle = \langle \chi_3 \rangle$. Departure from this equality provides an estimate of the error in $\langle \chi_3 \rangle$. A mean SDR component ratio (P_{23}) is defined as $\langle \chi_2 \rangle / \langle \chi_3 \rangle$. Note, unlike K_{12}, P_{23} is not an anisotropy; rather it is a parameter that indicates error in χ_3.

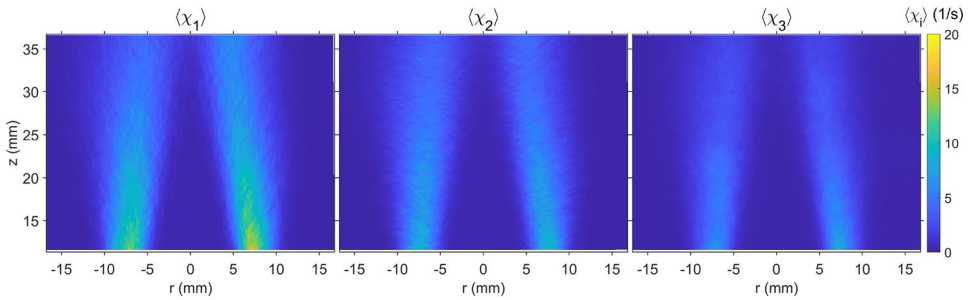

Fig. 11 Mean SDR components at mean laser-sheet separation $\Delta s = 304$ µm

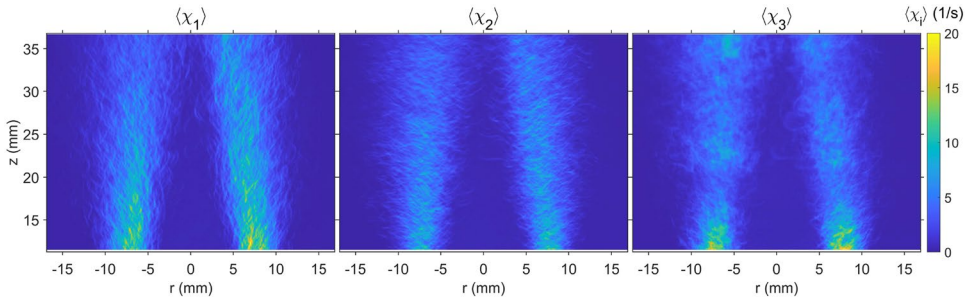

Fig. 12 Mean SDR components at mean $\Delta s = 140$ µm

P_{23} is evaluated at the identical three axial zones as stated previously. The area-averaged P_{23} values are 1.36, 1.50, and 1.62, at the base, mid, and top zones, respectively, for mean $\Delta s = 304$ µm. A possible reason for the increase in P_{23} with height can be attributed to the increased fluctuations of X_f owing to the central jet interaction with the annular swirling coflow. Overall, the departure of P_{23} from unity is significant. Thus, $\Delta s = 0.3$ mm is insufficient to resolve X_f gradients in x_3 direction. Therefore, Δs needs to be reduced further. As observed from instantaneous χ_i images in Fig. 10, Δs around 0.15 mm appears to be sufficient to resolve χ_3. Thus, another dataset containing 1600 image pairs was acquired with mean $\Delta s = 109$ µm, where due to shot-to-shot laser instability, Δs fluctuated between 55 to 165 µm. From this data, the global (averaged over the entire FOV) value of P_{23} is found to be 0.67. This implies that χ_3 is overestimated owing to noise or minute errors in X_f, which gets amplified in SDR, especially at lower Δs. Systematic errors/biases also affect χ_3. Since Δs for each realization is known, we select images in a range of $\Delta s = 135$ to 165 µm, with the mean value of 140 µm. The mean SDR components from this dataset are shown in Fig. 12. Only 165 realizations (out of 1600) were within the desired Δs range. Consequently, mean SDR components shown in Fig. 12 are less converged. The global P_{23} for the $\Delta s = 140$ µm subset is 0.94, which is close to the expected value. Regional values of P_{23} are evaluated at three axial locations in an identical manner as described previously. At the base, P_{23} is 0.72, which indicates overestimation of χ_3. At mid and top regions, P_{23} is 1.02 and 0.96, respectively, which suggests χ_3 can be measured accurately with $\Delta s \approx 0.15$ mm. The explanation for this optimal Δs value is provided next in terms of the Batchelor scale. Recall, the resolution requirement for two-point differenced χ_3 is not as stringent as centrally differenced in-plane SDR components.

3.3 PDF of SDR components

Significant intermittency exists in the SDR field. Therefore, a comparison of χ_i based on the mean may only provide partial insights. Alternatively, the probability density function (PDF) of χ_i can be evaluated. PDF approach is beneficial since it preserves instantaneous representation while making use of all the available images, rather than a few samples (as in Fig. 10).

PDF is evaluated for each component of SDR. χ_i values over the entire FOV are considered while evaluating PDF. Data is divided into 100 bins. Figure 13a shows PDFs of χ_i for the mean $\Delta s = 304$ µm dataset. For a given PDF amplitude, $\chi_1 > \chi_2$, which confirms the anisotropy of the flow. The χ_3 component is substantially lower than χ_2, indicating that the X_f gradients in the x_3 direction are not properly resolved. PDFs for mean $\Delta s = 109$ µm dataset

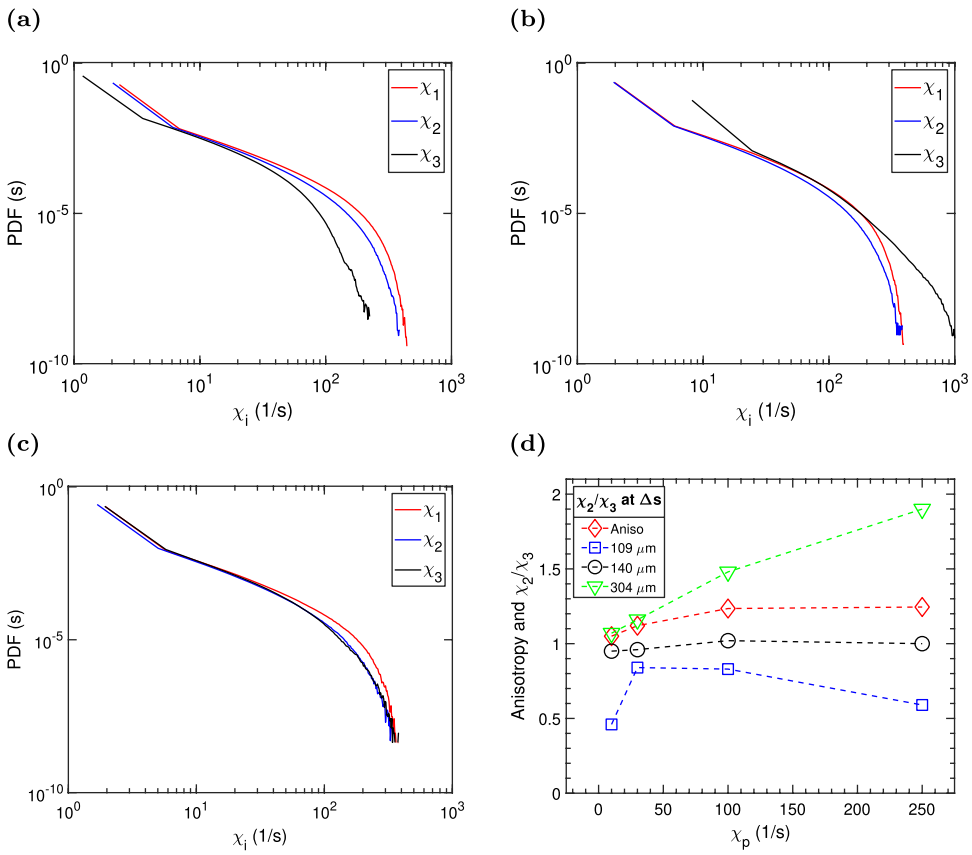

Fig. 13 Effect of laser-sheet spacing on PDF, P(χ_i) at mean: **a** $\Delta s = 304$ µm **b** $\Delta s = 109$ µm, and **c** $\Delta s = 140$ µm. **d** PDF-based anisotropy between χ_1 and χ_2, and validation of χ_3 at different Δs

are shown in Fig. 13b. The in-plane SDR component ratio, χ_1/χ_2, is identical to that of $\Delta s = 304$ µm dataset, as expected. However, the χ_3 component is consistently higher than χ_2, which suggests possible noise and systematic bias influences on the gradients of X_f in the x_3 direction. PDFs for the optimized mean $\Delta s = 140$ µm dataset are shown in Fig. 13c. In this plot, PDFs of χ_2 and χ_3 are in very close agreement. PDF data is further analyzed to quantify the anisotropy (χ_1/χ_2) and the extent of agreement between χ_2 and χ_3.

For a given PDF amplitude, the ratio of χ_1/χ_2 is evaluated to deduce anisotropy. This quantity is denoted as K^p_{12}. Ratios at four PDF amplitudes corresponding to the probe SDR values (χ_p) of $\chi_1 = 10$, 30, 100, and 250 s^{-1} are obtained. To reduce uncertainty in K^p_{12}, PDF is fitted with a piecewise polynomial, and the χ_i values are interpolated. Figure 13d shows the plot of K^p_{12} (i.e., PDF-based anisotropy) as a function of χ_p. At lower SDR values, χ_i components are nearly isotropic. Anisotropy increases to 1.2 at $\chi_p = 100\ s^{-1}$. A near-plateau is observed in K^p_{12} with a further increase in χ_p. In general, high SDR structures are observed to be anisotropic. Next, to validate the χ_3 component, ratio of $\chi_2/\chi_3 = 1$, serves as a reference with axial-azimuthal isotropy assumption. Similar to anisotropy, χ_2/χ_3 ratio at four χ_p values is considered. This ratio is denoted as P^p_{23}. For P^p_{23} evaluation, χ_2 values between 10 to 250 s^{-1} are used as probe SDR locations. For mean $\Delta s = 304$ µm, P^p_{23} value is near unity at low SDR values. P^p_{23} increases with SDR intensity in a quasi-linear manner. The deviation of P^p_{23} from unity is attributed to the underestimation of χ_3 due to an under-resolved mixing field in the out-of-plane direction. On the other hand, over-resolution (when laser sheets are too close) produces an overestimation of χ_3, as evidenced by $P^p_{23} < 1$ for $\Delta s = 109$ µm. For this case, P^p_{23} varies non-monotonically with SDR. For the optimized $\Delta s = 140$ µm dataset, P^p_{23} approaches near-unity over the entire range of χ_p. As χ_p increases from 10 to 250 s^{-1}, the ratio varies from 0.95 to 1. In this manner, quantification of SDR anisotropy and validation of χ_3 are achieved. For the mean analysis (Sect. 3.2.2), quantification is performed as a function of the spatial location, whereas the PDF-based quantification is conditioned on SDR values. Overall, the PDF analysis confirms the finding deduced from the mean χ_i analysis.

So far, through the analysis of instantaneous, mean, and PDF results, we have demonstrated that there exists an optimum laser-sheet separation distance that can provide an accurate estimate of the out-of-plane SDR component. The optimum value of $\Delta s = 140$ µm is larger than the estimated Batchelor scale, $\lambda_B = 56$ µm. As discussed in Sect. 3.2.1, Δs

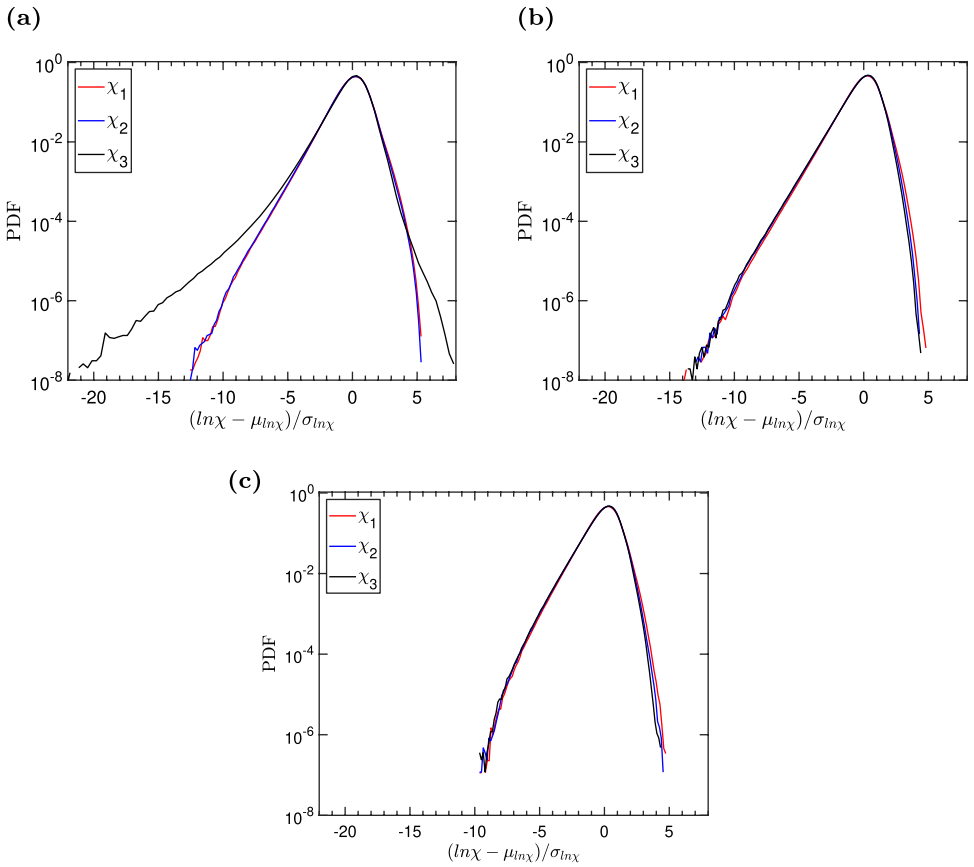

Fig. 14 Effect of laser-sheet spacing on PDF of normalized χ_i at mean: **a** $\Delta s = 304$ µm **b** $\Delta s = 109$ µm, and **c** $\Delta s = 140$ µm

need not match λ_B. Depending on the random noise, systematic biases, and differencing stencil, Δs can generally be 2 to 3 times λ_B. The present optimum Δs value is $2.5\lambda_B$. Note, unlike fine wire probes, Δs between laser sheets could not be precisely obtained due to finite sheet thickness and spatial overlap between two sheets. This aspect also influences the optimum Δs value, in addition to the noise and systematic bias characteristics of a given measurement. The use of two-point differencing also results in a less stringent resolution requirement relative to the central differencing stencil.

In the preceding sections, we discussed the impact of over-resolution on χ_3. In principle, over-resolution should not alter χ_3. We postulated that random errors in X_f due to a finite SNR propagates while evaluating χ_3, along with systematic biases. To further examine this aspect, a fluctuating component of χ_i is deduced. Similar to Soulopoulos et al. (2015), a mean-subtracted normalized fluctuating component of χ_i is obtained as, $\chi_N = \left(\hat{\chi} - \mu_{\hat{\chi}}\right)/\sigma_{\hat{\chi}}$, where $\hat{\chi} = \ln(\chi)$, μ is the local mean, and σ is the local standard deviation. Such normalization tends to remove systematic biases in the measurement through mean subtraction. The deduced PDFs of χ_N are shown in Fig. 14. For the mean $\Delta s = 304$ µm dataset, the PDF shape of χ_3 in Fig. 14a deviates substantially from the in-plane SDR components due to unresolved mixing scales. For mean $\Delta s = 140$ µm dataset in Fig. 14c, PDF shapes of all three SDR components are in agreement. The identical agreement is observed even for mean $\Delta s = 109$ µm dataset in Fig. 14b. Note, for

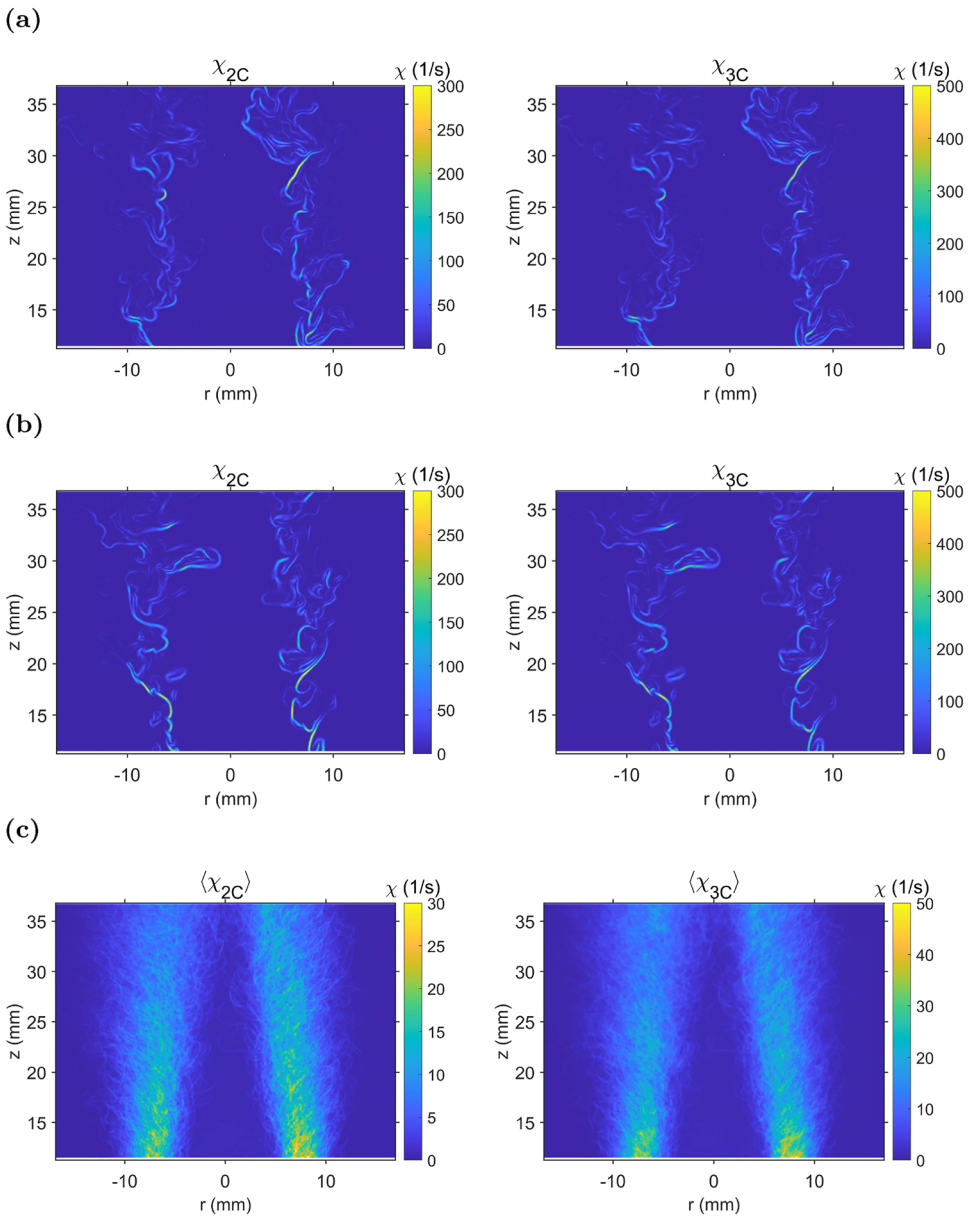

Fig. 15 SDR field containing two and three components: **a**, **b** Instantaneous SDR for $\Delta s = 143$ µm, and **c** Mean SDR for mean $\Delta s = 140$ µm

$\Delta s = 109$ µm data, PDFs of absolute SDR components, χ_2 and χ_3 (Fig. 13b) do not show agreement. The agreement of normalized χ_i PDFs and disagreement of absolute χ_i PDFs suggests that the absolute SDR is affected by systematic errors/biases. Finer Δs (than the optimized 140 µm) could be used if only the normalized fluctuating component of SDR is of interest which is typically the case in the turbulence community. However, for instantaneous absolute SDR estimation, Δs needs to be optimized through the approach described in this study.

3.4 Full three-component SDR

Now that we have rigorously validated the SDR measurements, we present the full SDR field by accounting for all three components. Based on the above analysis, we choose the data only around the optimum Δs. Figure 15 shows two samples of instantaneous two-component (χ_{2C}) and three-component (χ_{3C}) SDR with $\Delta s = 143$ µm. The spatial structures of χ_{2C} and χ_{3C} are quite similar with a nearly identical thickness of SDR layers; however, the values differ considerably. Out of the 1600 realizations, around 52 instances occur with $\Delta s \approx 143$ µm. These 52 SDR fields are averaged. We use this ensemble-averaged data to quantify the difference between two- and three-component SDR at a given Δs. Two regions of interest (ROIs) are identified at the bottom and top heights along the shear layer. ROI of 4×4 mm^2 centered around a given radius (r) and axial distance (z) is considered. The larger ROI was needed due to limited samples. The values of (r, z) in mm are (8, 12) for bottom ROI and (5, 36) for top ROI. Within these regions, SDR values are area-averaged. This ensemble- and area-averaged SDR is used as a characteristic value for a given ROI. Such averaging reduces the convergence uncertainty. The convergence with respect to the number of samples is presented in the appendix (Fig. 18a). The values are converged within 2%. The mean χ_{3C}/χ_{2C} ratio measures around 1.61 at the bottom ROI and 1.47 at the top ROI. For the overall field, the χ_{3C}/χ_{2C} ratio is 1.54. This ratio should have been less than 1.5 owing to the axial-azimuthal SDR isotropy assumption based Δs optimization. Note, this optimization deduced through mean and PDF data is global in nature. In the mean-based analysis, SDR data is conditioned on spatial location, whereas in the PDF-based analysis, SDR data is conditioned on SDR intensity. In both the analyses, SDR data within the entire FOV was considered, and thus, it leads to global optimization of Δs. Nonetheless, the optimized Δs is within the recommended limit of $2 - 3\lambda_B$. Therefore, the azimuthal component of SDR is considered to be resolved. Consequently, the local SDR isotropy can be inferred by comparing SDR components. For the base region of the flow, radial-azimuthal isotropy is noted (i.e., $\chi_1 \approx \chi_3$, within $2 - 3\%$). The interaction between the central jet and swirling co-flow near the jet exit is expected to be stronger. Consequently, χ_{3C}/χ_{2C} ratio is greater than 1.5. In the downstream region, axial-azimuthal quasi-isotropy is noted ($\chi_2 \approx \chi_3$, within 10%). The azimuthal component of SDR measures higher than its axial counterpart. Anisotropy ratios are provided subsequently.

Next, we compare mean fields of χ_{2C} and χ_{3C} in Fig. 15c. These plots are obtained using the mean $\Delta s = 140$ µm subset where instantaneous Δs ranges from 135 to 165 µm. Although only 165 realizations are accessible, the mean is converged within 1%, as observed from Fig. 18b. Both the mean χ_{2C} and χ_{3C} distributions appear identical, but as expected, mean χ_{3C} values are higher. The ensemble- and area-averaged value of χ_{3C}/χ_{2C} ratio is evaluated for the identical bottom and top locations as of 52 sample subset analysis. Since more (165) samples are available for averaging, the ROI is reduced to 2×2 mm^2. χ_{3C}/χ_{2C} ratios are 1.60 at the bottom and 1.48 at the top, which are identical to the values obtained from the $\Delta s = 143$ µm dataset. In isotropic flows, χ_{3C}/χ_{2C} ratio is expected to be around 1.5, as discussed in the Introduction. We note a different value owing to anisotropy between SDR components. The anisotropy ratios are as follows. For the bottom ROI, $\chi_3/\chi_1 = 1.01$ and $\chi_3/\chi_2 = 1.45$. For the top ROI, $\chi_3/\chi_1 = 0.85$ and $\chi_3/\chi_2 = 1.10$. Recall that subscripts 1, 2, and 3 indicate radial, axial, and azimuthal components, respectively.

4 Concluding remarks

This study reports the direct measurement of fully 3D scalar dissipation rate (SDR) in a jet in turbulent swirling coflow configuration for the first time. Measurements were performed in a developing region of a high Reynolds number (Re = 24000) flow. The minimum Batchelor scale was estimated to be 56 µm. A dual-plane acetone-PLIF technique was employed to measure the mixing field in three dimensions. The influence of laser-sheet separation distance (Δs) on SDR was assessed meticulously through several approaches. Through this analysis, an optimum Δs was identified that could accurately measure the out-of-plane component of SDR (χ_3).

A Wiener filter-based noise reduction approach was demonstrated to reduce noise-induced errors in the SDR measurement. We showed that the in-plane spatial resolution needs to match the Batchelor scale to measure SDR accurately. Note, in the ideal case of noise-free data and absence of gradient-induced filtering, the resolution requirement is $\pi\lambda_B$ (Wang et al. 2007). The present requirement of $1\lambda_B$ is a consequence of using a central difference gradient stencil that requires better resolution.

The validation of χ_3 was achieved by assuming the isotropy between axial and azimuthal components of mean SDR. This assumption is based on the DNS study of a turbulent jet

(Vlad 2021). The comparison of instantaneous SDR components revealed the possibility of identifying the optimum Δs. If Δs is larger than the optimum value, χ_3 is underestimated, whereas smaller Δs leads to an overestimation of χ_3 owing to random errors and systematic biases in the measurement. The time-averaged or mean fields of SDR components were used to identify the appropriate value of Δs. $\Delta s = 0.14$ mm, approximately 2.5 times the Batchelor scale, was found to determine χ_3 accurately. This finding was further confirmed through the probability density function (PDF) based analysis of SDR components. Apart from PDFs of absolute SDR, PDFs of normalized fluctuating components of SDR were also analyzed. The normalized PDFs reveal that measurements with Δs even smaller than the identified optimum value could be used if the fluctuating component of SDR is of interest. This suggests the presence of systematic biases in χ_3 measurement. Through these validations, the full three-component instantaneous and mean SDR measurements were presented. The results showed that the two-component SDR measurement under-predicts the true values of the 3D SDR by a factor of 1.48 to 1.6. The following guidelines are provided for full 3D SDR deduction using the dual-plane laser-induced fluorescence technique. (a) Due to laser instability, it is necessary to monitor the sheet separation distance on a shot-to-shot basis. (b) Images need to be corrected for laser-sheet intensity profile, laser extinction, and shot noise. (c) To identify the required imaging resolution, an estimate of the Bachelor scale is necessary, which can be obtained from the dissipation spectrum. (d) The validation analysis can include a comparison of in-plane and out-of-plane SDR components. For this comparison, criteria based on time-averaged SDR and PDF of either absolute SDR or a normalized fluctuating component of SDR can be used.

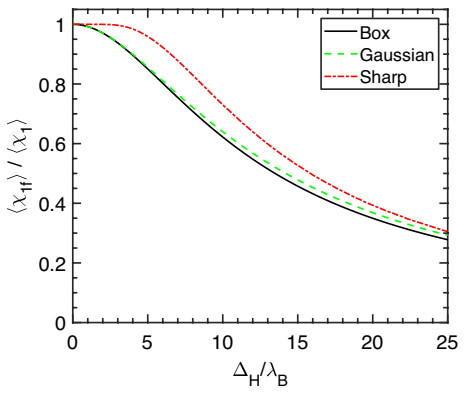

Fig. 16 Effect of spatial resolution on mean 1D SDR based on the model spectrum for $Re_\lambda = 164$

The present axial-azimuthal isotropy assumption could be validated through off-axis measurements.

Appendix 1

Resolution error curve

Figure 16 shows the effect of resolution on one-dimensional mean scalar dissipation rate. This curve is obtained using the model dissipation spectrum from Pope (2000) in an identical manner as of Wang et al. (2007b). The one-dimensional dissipation spectrum is filtered using the box, Gaussian, and sharp-spectral filters. The filter expressions can be found in Pope (2000) or Wang et al. (2007b). The mean SDR obtained from the unfiltered spectrum is denoted as $\langle\chi_1\rangle$, whereas its filtered counterpart is denoted as $\langle\chi_{1f}\rangle$. Δ_H is the characteristic filter width, and λ_B is the Bachelor length scale which is taken as 60 µm based on the dissipation spectrum presented in Fig. 6b. A crude estimate of the Taylor scale Reynolds number (Re_λ) is obtained by considering the longitudinal integral length scale, $L_{11} = 0.3$Da, where Da is the inner diameter of the outer tube. Next, the length scale used to evaluate the model spectrum is assumed to be $L = 0.5L_{11}$. Although the Re_λ (and corresponding spectrum) is uncertain due to the assumed scale, the resolution curve for SDR is not strongly sensitive to the Re_λ as shown by Wang et al. (2007b). Therefore, the above results can be used to obtain the resolution requirement for the present flow.

For the sharp-spectral filter, SDR can be obtained accurately even with the resolution of $3\lambda_B$, whereas for the box or Gaussian filtered data, the error at $3\lambda_B$ is $\approx 7\%$. For the resolution of $1\lambda_B$, the SDR accuracy of better than 1% can be achieved even with the box or Gaussian filtered data. Note that these findings are deduced from the noise-free modeled spectrum. For measurements, in addition to noise, the differencing stencil also influences the resolution requirement. Relative to the 2-point difference stencil, the resolution requirement for the 3-point central difference stencil is stringent (Wang et al. 2007b).

Appendix 2

Mean 2D SDR

See Fig. 17.

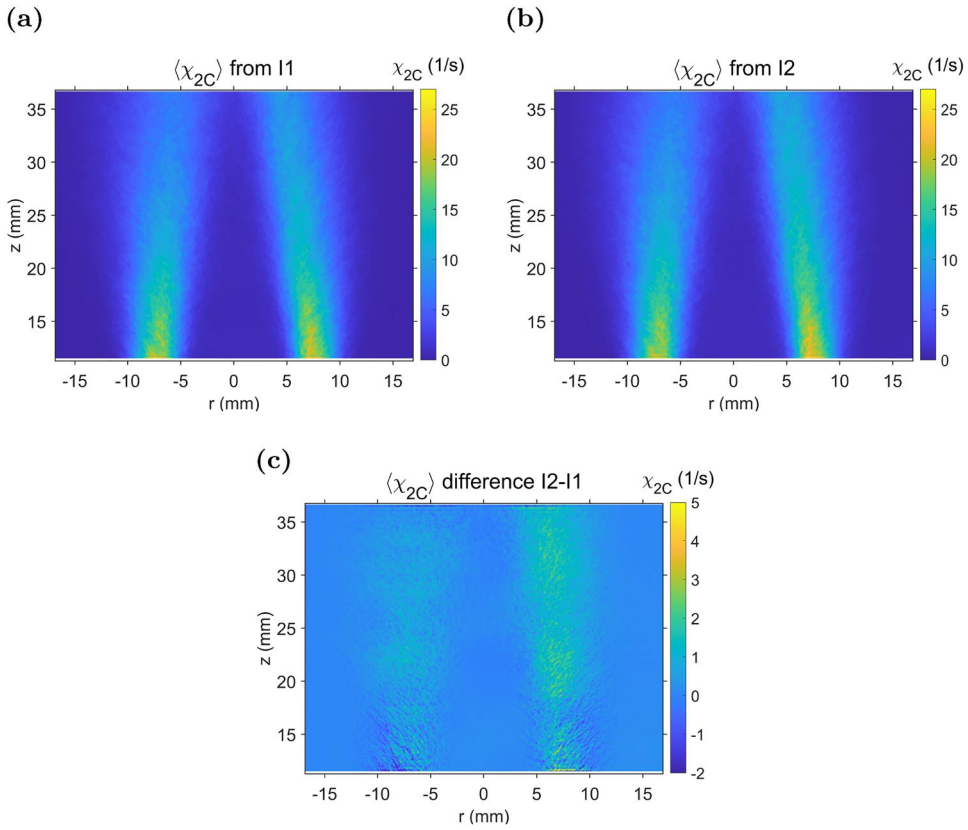

Fig. 17 Mean 2D SDR at mean $\Delta s = 109$ µm: **a** from I1 field of C1/L1 data at 9 mJ, and **b** from I2 field of C2/L2 data at 36 mJ, and **c** difference between SDR from I2 and I1

Appendix 3

Convergence

See Fig. 18.

Appendix 4

Energy and dissipation spectra

See Figs. 19 and 20.

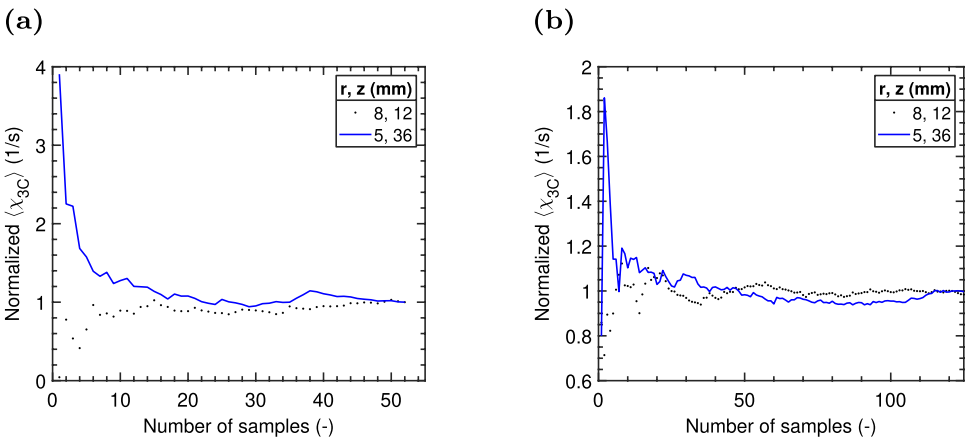

Fig. 18 Convergence of the ensemble- and area-averaged normalized χ_{3C} with the number of samples: **a** 52 samples with instantaneous $\Delta s = 143$ µm, and **b** 165 samples with mean $\Delta s = 140$ µm where instantaneous Δs ranges from 135 to 165 µm

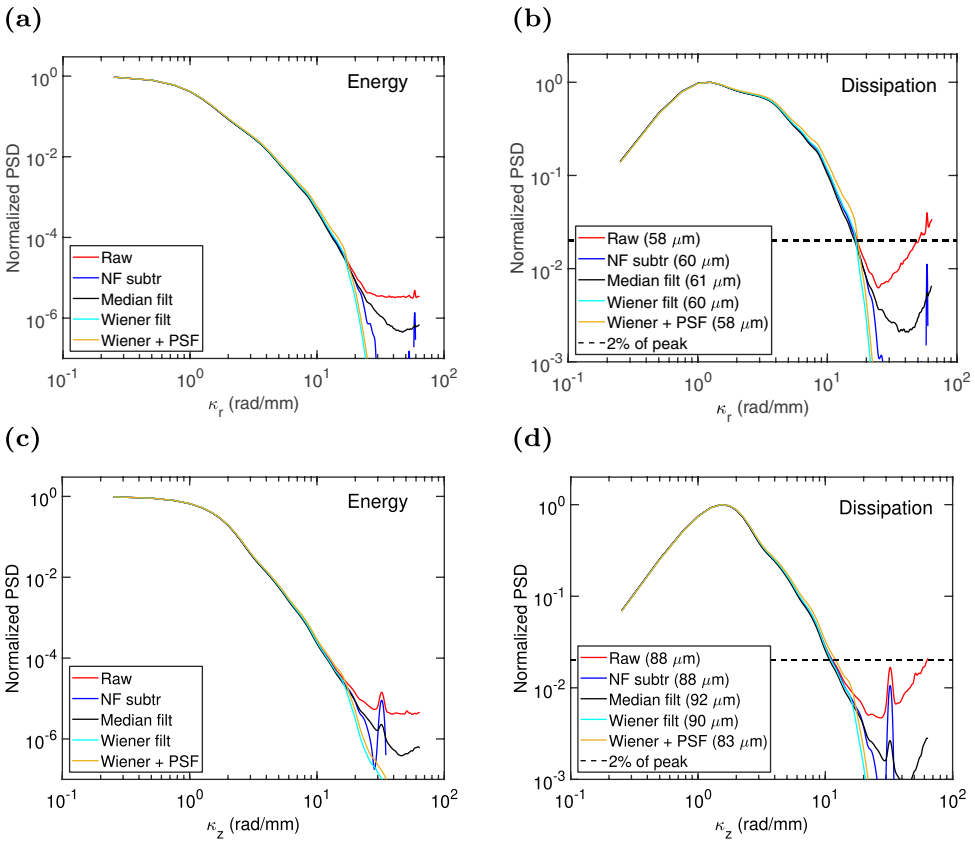

Fig. 19 Mean spectrum of fluctuating scalar, ζ', for the mid-ROI **a** radial energy, **b** radial dissipation, **c** axial energy, **d** axial dissipation. The Bachelor scale is indicated for each PSD curve

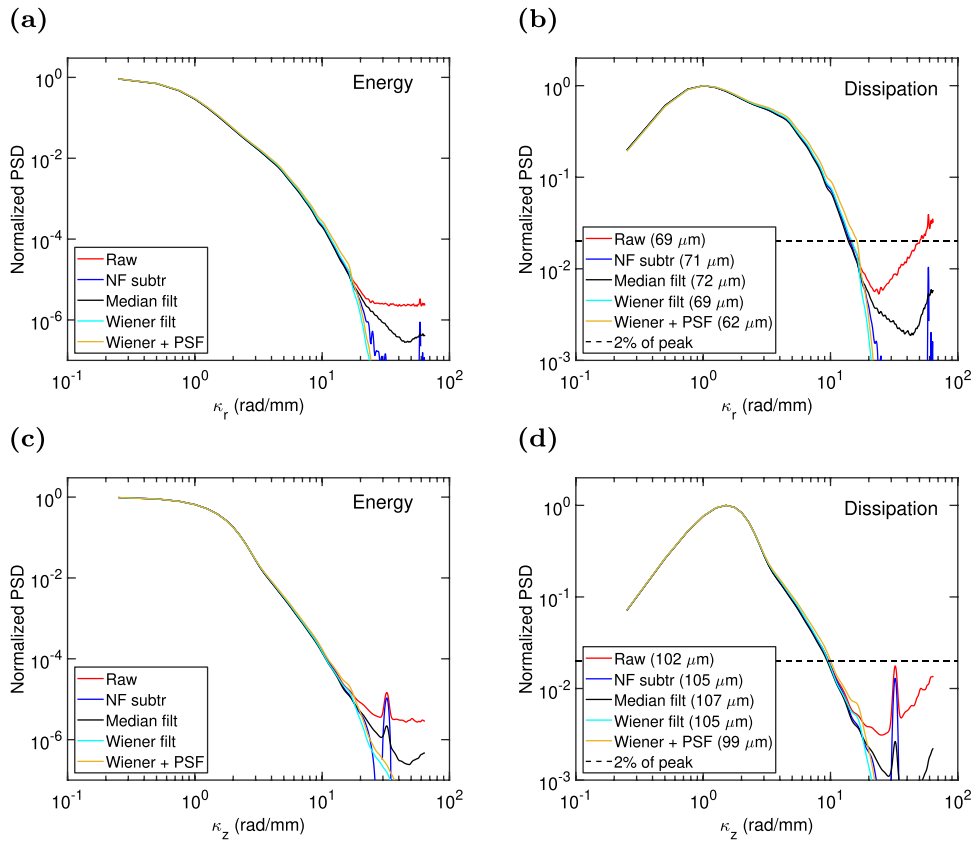

Fig. 20 Mean spectrum of fluctuating scalar, ζ', for the top ROI **a** radial energy, **b** radial dissipation, **c** axial energy, **d** axial dissipation. The Bachelor scale is indicated for each PSD curve

Acknowledgements The project (3DFlameGT) was funded by the European Commission under H2020-EU.1.3.2 scheme. Dr. I.A. Mulla acknowledges support through Marie Skłodowska-Curie Individual Fellowship (ID: 747576) awarded by the European Commission. The assistance of Dr. N. Soulopoulos and Dr. V. Stetsyuk in data processing is gratefully acknowledged. The authors also thank Dr. M. Gauding for helpful discussions.

Declarations

Conflict of interest The authors have no competing interests to declare that are relevant to the content of this article.

References

Antonia RA, Mi J (1993) Corrections for velocity and temperature derivatives in turbulent flows. Exp Fluids 14(3):203–208. https://doi.org/10.1007/bf00189511

Antonia RA, Mi J (1993) Temperature dissipation in a turbulent round jet. J Fluid Mech 250:531–551. https://doi.org/10.1017/s0022112093001557

Antonia RA, Satyaprakash BR, Hussain AKMF (1980) Measurements of dissipation rate and some other characteristics of turbulent plane and circular jets. Phys Fluids 23(4):695. https://doi.org/10.1063/1.863055

Barlow RS, Karpetis AN (2005) Scalar length scales and spatial averaging effects in turbulent piloted methane/air jet flames. Proc Combust Inst 30(1):673–680. https://doi.org/10.1016/j.proci.2004.08.139

Bijjula K, Kyritsis DC (2005) Experimental evaluation of flame observables for simplified scalar dissipation rate measurements in laminar diffusion flamelets. Proc Combust Inst 30(1):493–500. https://doi.org/10.1016/j.proci.2004.08.029

Bilger R (2004) Some aspects of scalar dissipation Flow Turbulence and Combustion formerly. Appl Sci Res 72(2–4):93–114. https://doi.org/10.1023/b:appl.0000044404.24369.f1

Buch KA, Dahm WJA (1996) Experimental study of the fine-scale structure of conserved scalar mixing in turbulent shear flows. Part 1. Sc $\gg$ 1. J Fluid Mech 317:21–71. https://doi.org/10.1017/s0022112096000651

Buch KA, Dahm WJA (1998) Experimental study of the fine-scale structure of conserved scalar mixing in turbulent shear flows. Part 2. Sc $\approx$ 1. J Fluid Mech 364:1–29. https://doi.org/10.1017/s0022112098008726

Chakraborty N, Kolla H, Sankaran R, Hawkes E, Chen J, Swaminathan N (2013) Determination of three-dimensional quantities related to scalar dissipation rate and its transport from two-dimensional measurements: Direct numerical simulation based validation. Proc Combust Inst 34(1):1151–1162. https://doi.org/10.1016/j.proci.2012.06.040

Chen J, Antonia R, Zhou Y, Zhou T (2020) Characteristics of temperature dissipation rate in a turbulent near wake. Exp Thermal Fluid Sci 114:110050. https://doi.org/10.1016/j.expthermflusci.2020.110050

Cutcher HC, Barlow RS, Magnotti G, Masri AR (2018) Statistics of scalar dissipation and reaction progress in turbulent flames with compositional inhomogeneities. Combust Flame 194:439–451. https://doi.org/10.1016/j.combustflame.2018.05.030

Dahm WJA, Buch KA (1989) Lognormality of the scalar dissipation pdf in turbulent flows. Phys Fluids A 1(7):1290–1293. https://doi.org/10.1063/1.857356

Dahm WJA, Southerland KB, Buch KA (1991) Direct, high resolution, four-dimensional measurements of the fine scale structure of Sc $\gg$ 1 molecular mixing in turbulent flows. Phys Fluids A 3(5):1115–1127. https://doi.org/10.1063/1.858093

Danaila L, Zhou T, Anselmet F, Antonia RA (2000) Calibration of a temperature dissipation probe in decaying grid turbulence. Exp Fluids 28(1):45–50. https://doi.org/10.1007/s003480050006

Dimotakis PE (2005) Turbulent Mixing. Annu Rev Fluid Mech 37(1):329–356. https://doi.org/10.1146/annurev.fluid.36.050802.122015

Feikema DA, Everest D, Driscoll JF (1996) Images of dissipation layers to quantify mixing within a turbulent jet. AIAA J 34(12):2531–2538. https://doi.org/10.2514/3.13435

Frackowiak B, Strzelecki A, Lavergne G (2008) A liquid–vapor interface positioning method applied to PLIF measurements around evaporating monodisperse droplet streams. Exp Fluids 46(4):671–682. https://doi.org/10.1007/s00348-008-0592-3

Frank JH, Kaiser SA (2007) High-resolution imaging of dissipative structures in a turbulent jet flame with laser rayleigh scattering. Exp Fluids 44(2):221–233. https://doi.org/10.1007/s00348-007-0396-x

Fuest F, Barlow RS, Magnotti G, Sutton JA (2018) Scalar dissipation rates in a turbulent partially-premixed dimethyl ether/air jet flame. Combust Flame 188:41–65. https://doi.org/10.1016/j.combustflame.2017.09.020

Ghandhi JB (2006) Spatial resolution and noise considerations in determining scalar dissipation rate from passive scalar image data. Exp Fluids 40(4):577–588. https://doi.org/10.1007/s00348-005-0097-2

Hawkes ER, Sankaran R, Chen JH, Kaiser SA, Frank JH (2009) An analysis of lower-dimensional approximations to the scalar dissipation rate using direct numerical simulations of plane jet flames. Proc Combust Inst 32(1):1455–1463. https://doi.org/10.1016/j.proci.2008.06.122

Hsu A, Narayanaswamy V, Clemens N, Frank J (2011) Mixture fraction imaging in turbulent non-premixed flames with two-photon LIF of krypton. Proc Combust Inst 33(1):759–766. https://doi.org/10.1016/j.proci.2010.06.051

Kaiser SA, Frank JH (2007) Imaging of dissipative structures in the near field of a turbulent non-premixed jet flame. Proc Combust Inst 31(1):1515–1523. https://doi.org/10.1016/j.proci.2006.08.043

Kaiser SA, Frank JH (2011) The effects of laser-sheet thickness on dissipation measurements in turbulent non-reacting jets and jet flames. Meas Sci Technol 22(4):045403. https://doi.org/10.1088/0957-0233/22/4/045403

Karpetis A, Barlow R (2002) Measurements of scalar dissipation in a turbulent piloted methane/air jet flame. Proc Combust Inst 29(2):1929–1936. https://doi.org/10.1016/s1540-7489(02)80234-6

Karpetis AN, Barlow RS (2005) Measurements of flame orientation and scalar dissipation in turbulent partially premixed methane flames. Proc Combust Inst 30(1):665–672. https://doi.org/10.1016/j.proci.2004.08.222

Kothnur PS, Clemens NT (2005) Effects of unsteady strain rate on scalar dissipation structures in turbulent planar jets. Phys Fluids 17(12):125104. https://doi.org/10.1063/1.2136827

Krawczynski JF, Renou B, Danaila L, Demoulin FX (2006) Small-scale measurements in a partially stirred reactor. Exp Fluids 40(5):667–682. https://doi.org/10.1007/s00348-005-0099-0

Lilley DG (1977) Swirl flows in combustion: A review. AIAA J 15(8):1063–1078. https://doi.org/10.2514/3.60756

Markides C, Mastorakos E (2006) Measurements of scalar dissipation in a turbulent plume with planar laser-induced fluorescence of acetone. Chem Eng Sci 61(9):2835–2842. https://doi.org/10.1016/j.ces.2005.10.040

Mi J, Nathan G (2003) The influence of probe resolution on the measurement of a passive scalar and its derivatives. Exp Fluids 34(6):687–696. https://doi.org/10.1007/s00348-003-0603-3

Mi J, Antonia RA, Anselmet F (1995) Joint statistics between temperature and its dissipation rate components in a round jet. Phys Fluids 7(7):1665–1673. https://doi.org/10.1063/1.868484

Miller PL, Dimotakis PE (1991) Stochastic geometric properties of scalar interfaces in turbulent jets. Phys Fluids A 3(1):168–177. https://doi.org/10.1063/1.857876

Miller PL, Dimotakis PE (1996) Measurements of scalar power spectra in high schmidt number turbulent jets. J Fluid Mech 308:129–146. https://doi.org/10.1017/s0022112096001425

Milosavljevic VD (1993) Natural gas, kerosene and pulverised fuel fired swirl burners. PhD thesis. University of London

Namazian M, Schefer R, Kelly J (1988) Scalar dissipation measurements in the developing region of a jet. Combust Flame 74(2):147–160. https://doi.org/10.1016/0010-2180(88)90013-2

Papageorge M, Sutton JA (2017) Intrusive effects of repetitive laser pulsing in high-speed tracer-LIF measurements. Exp Fluids. https://doi.org/10.1007/s00348-017-2323-0

Park O, Burns RA, Clemens NT (2019) Relationship between soot and scalar dissipation rate in the soot-inception region of turbulent non-premixed jet flames. Proc Combust Inst 37(1):1057–1064. https://doi.org/10.1016/j.proci.2018.06.174

Peters N (1983) Local quenching due to flame stretch and non-premixed turbulent combustion. Combust Sci Technol 30(1–6):1–17. https://doi.org/10.1080/00102208308923608

Peters N (1988) Laminar flamelet concepts in turbulent combustion. In: Symposium (International) on combustion, vol 21, no 1, pp 1231–1250. https://doi.org/10.1016/s0082-0784(88)80355-2

Petersen B, Ghandhi J (2011) High-resolution turbulent scalar field measurements in an optically accessible internal combustion engine. Exp Fluids 51(6):1695–1708. https://doi.org/10.1007/s00348-011-1178-z

Pope SB (2000) Turbulent Flows. Cambridge University Press, Cambridge. https://doi.org/10.1017/CBO9780511840531

Renfro MW, Gore JP, King GB, Laurendeau NM (2000) Self-similarity of hydroxyl-concentration temporal statistics in turbulent non-premixed jet flames. AIAA J 38(7):1230–1236. https://doi.org/10.2514/2.1092

Slessor MD, Bond CL, Dimotakis PE (1998) Turbulent shear-layer mixing at high reynolds numbers: effects of inflow conditions. J Fluid Mech 376:115–138. https://doi.org/10.1017/s0022112098002857

Smith SW (1997) The Scientist and Engineer's Guide to Digital Signal Processing. California Technical Publishing, USA

Soulopoulos N, Hardalupas Y, Taylor AMKP (2014) Scalar dissipation rate measurements in a starting jet. Exp Fluids. https://doi.org/10.1007/s00348-014-1685-9

Soulopoulos N, Hardalupas Y, Taylor AMKP (2015) Mixing and scalar dissipation rate statistics in a starting gas jet. Phys Fluids 27(12):125103

Stårner S, Bilger R, Lyons K, Frank J, Long M (1994) Conserved scalar measurements in turbulent diffusion flames by a raman and rayleigh ribbon imaging method. Combust Flame 99(2):347–354. https://doi.org/10.1016/0010-2180(94)90140-6

Stetsyuk V (2014) Experimental study of combustion and scalar mixing in swirling jet flows. PhD thesis. Imperial College London

Stetsyuk V, Soulopoulos N, Hardalupas Y, Taylor AMKP (2016) Scalar dissipation rate statistics in turbulent swirling jets. Phys Fluids 28(7):075104. https://doi.org/10.1063/1.4954657

Su L, Clemens N (1999) Planar measurements of the full three-dimensional scalar dissipation rate in gas-phase turbulent flows. Exp Fluids 27(6):507–521. https://doi.org/10.1007/s003480050375

Sutton JA, Driscoll JF (2013) Measurements and statistics of mixture fraction and scalar dissipation rates in turbulent non-premixed jet flames. Combust Flame 160(9):1767–1778. https://doi.org/10.1016/j.combustflame.2013.03.006

Tsurikov M, Clemens N (2002) The structure of dissipative scales in axisymmetric turbulent gas-phase jets. In: 40th AIAA aerospace sciences meeting & exhibit. American institute of aeronautics and astronautics. https://doi.org/10.2514/6.2002-164

Unterleitner FC, Hormats EI (1965) Rates of decay of phosphorescence from triphenylene in acrylic polymers. J Phys Chem 69(8):2516–2520. https://doi.org/10.1021/j100892a005

Vlad AS (2021) Investigation on spatial and temporal characteristics of scalar dissipation rate in non-reacting and reacting turbulent jets. PhD thesis. The University of Edinburgh. https://doi.org/10.7488/ERA/1204. https://era.ed.ac.uk/handle/1842/37929

Wagner B, Frackowiak B, Gajan P, Strzelecki A (2009) Fuel vapor concentration measurements by laser induced fluorescence and infra-red extinction: an investigation on a monodisperse droplet stream. In: Volume 2: Combustion, Fuels and Emissions. ASMEDC. https://doi.org/10.1115/gt2009-59949

Wang G, Barlow RS (2007) Spatial resolution effects on the measurement of scalar variance and scalar gradient in turbulent nonpremixed jet flames. Exp Fluids 44(4):633–645. https://doi.org/10.1007/s00348-007-0423-y

Wang G, Karpetis AN, Barlow RS (2007) Dissipation length scales in turbulent nonpremixed jet flames. Combust Flame 148(1–2):62–75. https://doi.org/10.1016/j.combustflame.2006.09.005

Wang GH, Barlow R, Clemens N (2007) Quantification of resolution and noise effects on thermal dissipation measurements in turbulent non-premixed jet flames. Proc Combust Inst 31(1):1525–1532. https://doi.org/10.1016/j.proci.2006.07.242

Wang GH, Clemens NT, Barlow RS, Varghese PL (2007) A system model for assessing scalar dissipation measurement accuracy in turbulent flows. Meas Sci Technol 18(5):1287–1303. https://doi.org/10.1088/0957-0233/18/5/015

Wyngaard JC (1971) Spatial resolution of a resistance wire temperature sensor. Phys Fluids 14(9):2052. https://doi.org/10.1063/1.1693718

Yaws CL (2009) Diffusion coefficient in air - organic compounds. Transport Properties of Chemicals and Hydrocarbons. Elsevier, Amsterdam, pp 407–496. https://doi.org/10.1016/b978-0-8155-2039-9.50015-6

Yip B, Long MB (1986) Instantaneous planar measurement of the complete three-dimensional scalar gradient in a turbulent jet. Opt Lett 11(2):64. https://doi.org/10.1364/ol.11.000064